Three-dimensional attenuation tomography at Loma Prieta: Inversion of t^* for Q

Jonathan M. Lees

Department of Geology and Geophysics, Yale University, New Haven, Connecticut

Grant T. Lindley

Institute for Crustal Studies, University of California, Santa Barbara

Abstract. Three-dimensional Q^{-1} variations in the aftershock region of Loma Prieta are derived by tomographic inversion. The data set consists of over 4000 aftershock recordings at 22 PASSCAL (Program for Array Seismic Studies of the Continental Lithosphere) stations deployed after the Loma Prieta mainshock of 1989. Estimates of attenuation are determined from nonlinear least squares best fits to the Fourier amplitude spectrum of P and S wave arrivals. The linear attenuation inversion is accomplished by using three-dimensional velocity variations derived previously in nonlinear velocity inversions. Low Q is observed near the surface and Q generally increases with depth. The southwest side of the San Andreas fault exhibits lower Q than does the northeast side and this feature apparently extends to approximately 7 km depth. The fault zone, as determined by the dipping plane of aftershock activity, is characterized by slightly higher Q_P and lower Q_S, compared to regions immediately adjacent to the fault. These correlate with high-velocity anomalies associated with seismicity at depth. The results are in agreement with earlier observations regarding the association of high-velocity anomalies, seismicity, and fault zone asperities.

Introduction

Attenuation tomography has been applied previously to active source data sets [Clawson et al., 1989; Evans and Zucca, 1988] and to data derived from earthquakes [Ho-Liu et al., 1988; Scherbaum, 1990; Scherbaum and Wyss, 1990; Young and Ward, 1980]. These studies are concentrated mostly on volcanic regions where our a priori models are relatively simple, that is, zones of large magma accumulation are expected to have high attenuation and low velocity . In the case of fault zones a similar situation exists; along the fault gouge we expect to observe low velocity and high attenuation due to extensive fracturing, crack accumulation, and partial saturation [Wittlinger et al., 1983]. In the case of fault zones, however, variations in lithology may have a considerable influence on propagation properties making such simple, a priori, models speculative at best. In the Parkfield, California, region, attenuation of high-frequency seismic waves has been observed to vary by at least a factor of 2 laterally along the fault and by a factor of 4-10 off the fault [Blakeslee, 1989; Blakeslee et al., 1989]. If similar lateral variations are present at Loma Prieta, the large volume of data recorded after the 1989 mainshock event provides a unique opportunity for determining three-dimensional variations of attenuation along the San Andreas fault.

The basic methods in this study are similar to those of Scherbaum [1990]. Our methods differ from Scherbaum's in the approach we have taken to solve both the nonlinear estimation of the source and attenuation parameters and in the tomographic inversion for three-dimensional Q structure. In our case we use an optimal global search method to find the best fit to the spectrum. This approach is more satisfying than the simple Levenburg-Marquardt approach used earlier because of the guarantee of global minimization. Furthermore, the tomographic inversion here utilizes the three-dimensional velocity structure previously derived using a nonlinear inversion and three-dimensional ray tracing.

We use previously derived three-dimensional P wave velocity tomography results in conjunction with spectral fits of P and S wave arrivals to model the Q structure in the Loma Prieta region. Earlier studies have observed a high correlation of fault seismicity with high-velocity regions in this area, and we would like to know if the high-velocity zones also represent material whose attenuation is anomalously high or low. If we can determine this, we may be able to differentiate between various interpretations of the tomographic anomalies: is the high velocity associated with stress related anomalies along the fault [Lees, 1990; Lees and Malin, 1990; Nicholson and Lees, 1992b] or is it lithologic, as suggested by Shalev and Lees [1994]?

Data and Methodology

The data in this study were selected from the 22 portable three-component PASSCAL (Program for Array Seismic Studies of the Continental Lithosphere) stations installed after the 1989 Loma Prieta earthquake. Figure 1 shows the named portable stations and other unnamed stations from the USGS permanent array. PASSCAL data were used because of their high quality and high data sample rate. The epicenters of the selected earthquakes are plotted on the map. Each PASSCAL record was
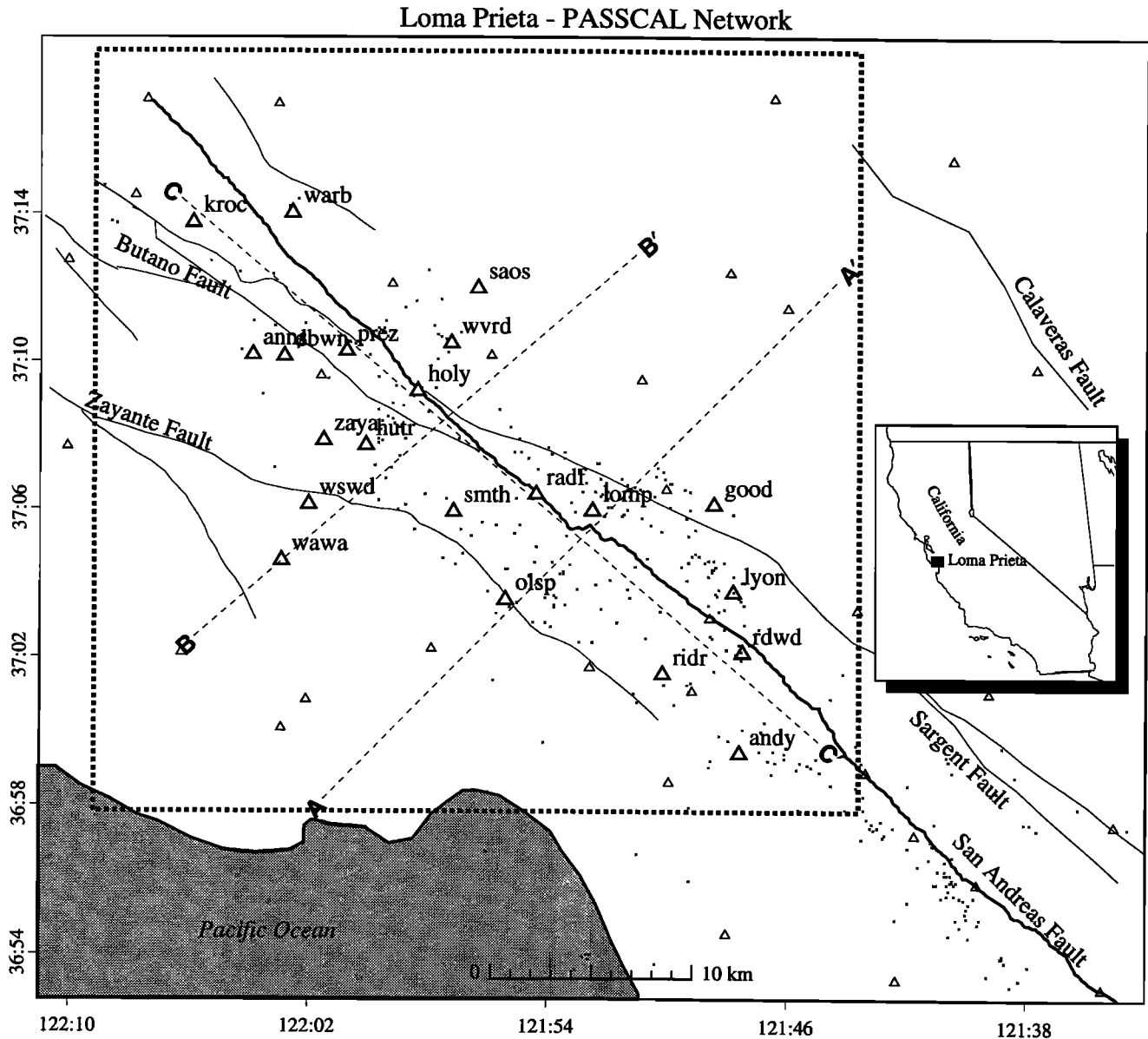
Loma Prieta - PASSCAL Network

Figure 1. Map of target area at Loma Prieta. Triangles with names represent the location of the PASSCAL (Program for Array Seismic Studies of the Continental Lithosphere) stations used in this study, and unnamed triangles are the location of U.S. Geological Survey permanent stations. Major faults and hypocenters are plotted for reference. Heavy dashed outline indicates the border of the three-dimensional tomographic analysis. Labeled lines AA', BB', and CC' are cross sections presented in Figures 9 and 11.

temporally associated with an event in the permanent U.S. Geological Survey (USGS) catalogue for purposes of determination of an earthquake location. The initial three-dimensional velocity model was determined using approximately 12,000 travel time records from the USGS array in a nonlinear tomographic inversion. The three-dimensional tomographic velocity inversion has been extensively studied by several researchers, and the major variations appear to be stable [*Eberhart-Phillips et al.*, 1990; *Lees*, 1990; *Lees and Shalev*, 1992; *Shalev and Lees*, 1992]. The primary structural features are a low velocity sedimentary block situated between the Sargent and Zayante faults and an apparent high-velocity wedge dipping along the trace of the seismicity below the San Andreas fault.

The underlying assumptions of the method used to determine attenuation in this study are based on the Brune source model [*Brune*, 1970; *Brune*, 1971], extended by *Boatwright* [1978], *Hanks and Wyss* [1972], *Madariaga* [1977], *Randall* [1973], and others. Assuming a model of the earthquake spectrum H(f) [*Boatwright*, 1978; *Lindley and Archuleta*, 1992],

$$H(f) = \frac{\Omega_0 \exp(-\pi f t^*)}{(1 + (\frac{f}{f_c})^{2\gamma})^{1/2}} \tag{1}$$

$$t^* = t_0^* f^{-\alpha} \tag{2}$$

where f is the frequency, Ω_0 is the amplitude at zero frequency,

f_C is the corner frequency, γ is the source spectral falloff, and t_0^* and α are parameters that determine attenuation. The approach is to window the P or S wave arrival, apply a 10% cosine taper, calculate the Fourier transform and, finally, window the frequency spectrum for model fitting. There are five free parameters in this model: t_0^*, Ω_0, f_C, α, and γ. It is impossible to find a unique best fit while allowing all five parameters to vary since there are many possible parameter combinations that will produce similar quality fits. In order to reduce the number of fit parameters, γ is assumed to be 2.0. The parameter γ measures the rate at which the spectrum falls off at high frequencies due to the source. In our case we have thus used the commonly assumed ω-square source model. The parameter α determines the frequency dependence of attenuation. Spectral fits were determined with α fixed at four different values: -1.0, -0.5, 0.0, and 0.5. The parameters Ω_0, f_C, and t_0^* were allowed to vary in the best fits to the Fourier spectra. The least squares best fits were determined using the simplex algorithm [*Caceci and*

Cacheris, 1984; *Nelder and Mead*, 1965]. Tomographic inversions for the four different values of α were found to be similar and we present only the inversion for $\alpha = 0.0$ (Q constant with frequency). Figures 2a-2f show examples of P wave and S wave spectral fits from the Loma Prieta data set.

The range of frequencies that could be analyzed was limited by noise, antialias filters, and the response of the instruments. For P waves, the noise was determined for each seismogram from the Fourier spectrum of a window placed just prior to the first P wave arrival. The range of frequencies fit was then determined by comparing the Fourier spectrum of the noise window to the P wave Fourier spectrum. Frequencies below the natural frequency of the sensors, 2 Hz, were not used. The highest frequency fit for P waves was typically 40 to 60 Hz, although some spectra could be fit to 80 Hz. Similar guidelines were used to determine the frequencies to fit for S waves. S waves were first rotated to transverse (SH) based on epicenter and station locations. The noise window for S waves was placed in the P wave coda just in
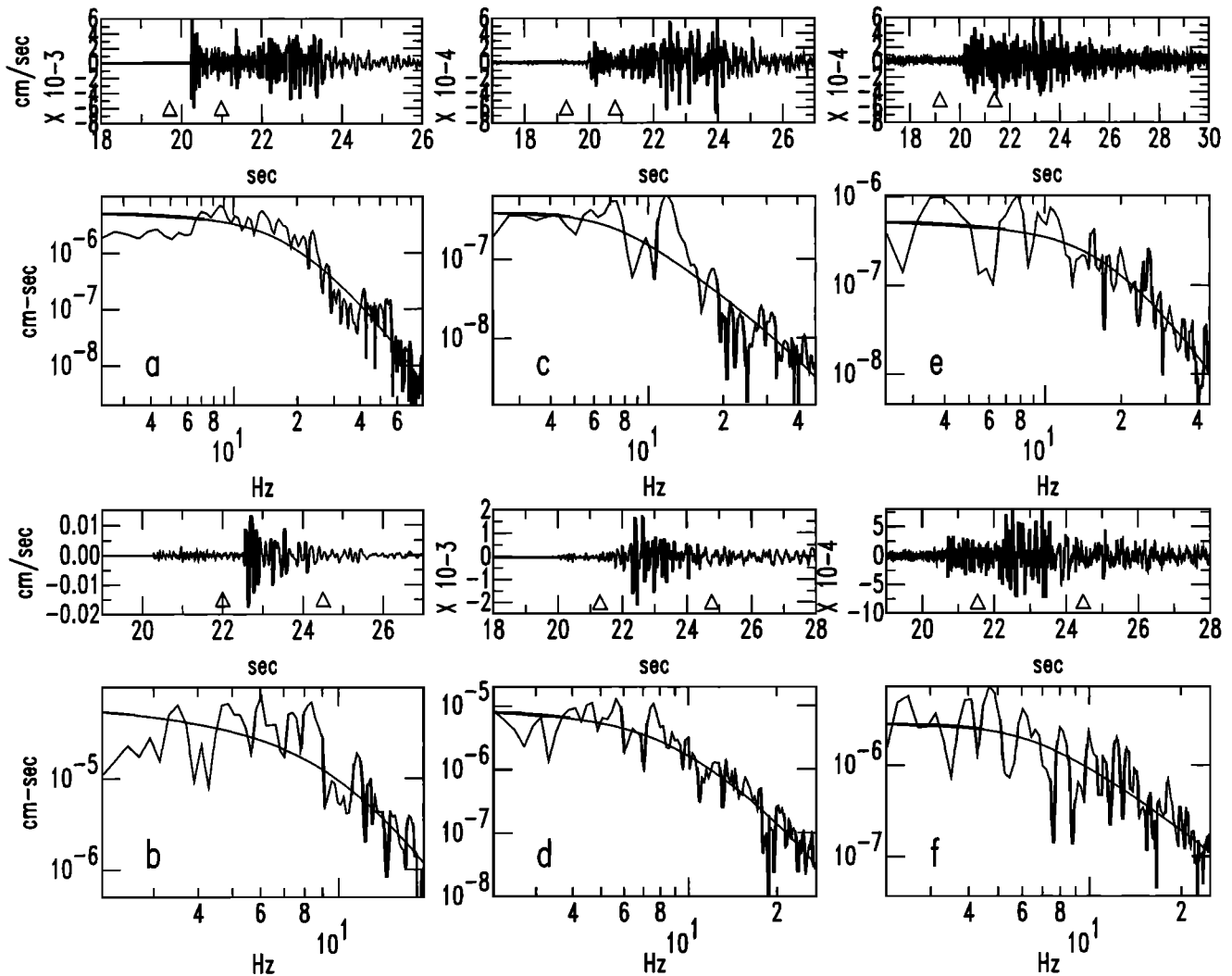

Figure 2. Examples of P and S wave windows and spectra. Triangles mark the windows for which the fast Fourier transforms were computed. Figures 2a, 2c, and 2e show P wave spectral fits from vertical components. Figures 2b, 2d, and 2f show S wave spectral fits from the horizontals rotated to the transverse component. The fit parameters are (a) $\Omega = 5.8 \times 10^{-6}$ cm s, $f_C = 15.6$ Hz, $t^* = 0.016$ s, (b) $\Omega = 7.7 \times 10^{-5}$ cm s, $f_C = 9.1$ Hz, $t^* = 0.052$ s, (c) $\Omega = 4.1 \times 10^{-7}$ cm s, $f_C = 7.1$ Hz, $t^* = 0.007$ s, (d) $\Omega = 1.1 \times 10^{-5}$ cm s, $f_C = 7.8$ Hz, $t^* = 0.039$ s, (e) $\Omega = 5.7 \times 10^{-7}$ cm s, $f_C = 15.7$ Hz, $t^* = 0.014$ s, (f) $\Omega = 3.0 \times 10^{-6}$ cm s, $f_C = 6.50$ Hz, $t^* = 0.008$ s.

front of the first S wave arrival. The noise (P wave coda) spectrum was generally observed to merge with the transverse S wave spectrum between 10 and 35 Hz depending on the recording. S wave spectra were not used if it appeared that the P wave coda dominated at frequencies below 10 Hz. This constraint limited the number of S wave t* values in the study.

One possible concern in the analysis is that t* may vary with window length. Window lengths were chosen to encompass most of the initial arriving energy and were typically 1.5 to 3.0 s for P waves and 2.5 to 5.0 s for S waves. Figures 3a and 3b show the variation of P and S wave t* with window length for one event (October 24, 0337:12 UT, 37°N 10.17', 122°W3.09') recorded at 10 different sites. P wave t* values are reasonably constant at

each of the sites for different window lengths. S wave t* values are also fairly constant for seven of the ten sites. For three of the sites, S wave t* values vary significantly for smaller window lengths (less than 3 s). The variation of t* with window length observed for some of the S wave recordings may be related to the smaller frequency ranges used in the spectral fits for S waves compared to P waves as discussed above.

The t* is then related to the quality factor Q by

$$t^* = \int\limits_{raypath} \frac{1}{Q(x,y,z)} \frac{1}{v(x,y,z)} dr(x,y,z) \qquad (3)$$

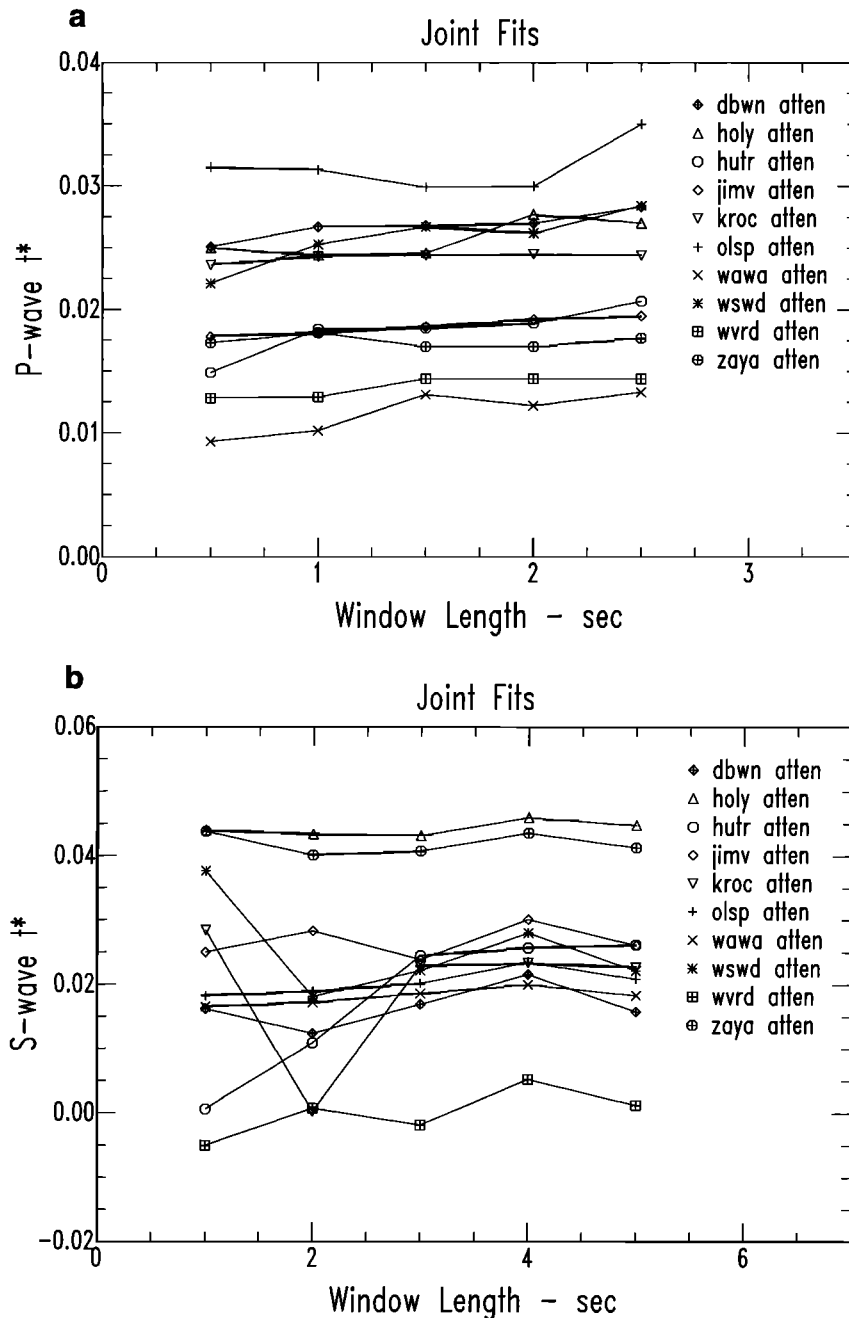where the integral is taken along the raypath of the seismic wave

Figure 3. Comparison of t* fitted values for one event using different window lengths. (a) P wave fits and (b) S wave fits. Note that t* estimates are generally consistent across a broad range of window lengths.

and Q and velocity (v) vary in three dimensions. Nonlinear tomographic analysis of P wave arrival times provides the three-dimensional variations of P wave velocity. Since no reliable, independent, three-dimensional S wave velocity model is available, the P wave model, scaled by $(3)^{1/2}$, was used for the S wave velocity. Three-dimensional ray tracing (based on ray bending [*Um and Thurber*, 1987]) is performed relative to the three-dimensional velocity models [*Lees and Shalev*, 1992]. Path effects associated with Q in equation (3) can be separated spatially in three dimensions by tomographic analysis. By path effects we include all sources of attenuation along the path, including intrinsic attenuation and scattering attenuation, or modification of the signals associated with focusing or defocusing [*Bregman et al.*, 1989]. While the first arrival ray path is a line through the model, the smoothing, introduced below, spreads the effect of the line integral in equation (1) over a finite volume along the ray. This volume represents a tube through which both scattering and intrinsic attenuation occur. Equation (3) is parameterized by small, discrete blocks within which the attenuation is assumed constant. The linear inversion is accomplished by solving the system:

$$\begin{bmatrix} \mathbf{A} \\ \lambda\mathbf{L} \end{bmatrix} \mathbf{Q}^{-1} = \begin{bmatrix} \mathbf{t}^* \\ \mathbf{0} \end{bmatrix}. \tag{4}$$

Where $\mathbf{A}$ is the matrix which describes the intersection of the raypaths with the block model, $\mathbf{L}$ is a two-dimensional Laplacian operator used to regularize the inversion, λ is a damping parameter which controls the relative weight of adhering to the data versus constraining the Laplacian of the model to be small, and $\mathbf{t}^*$ is a vector of t^* values estimated from the nonlinear spectral inversion. The bold symbol $\mathbf{Q}^{-1}$ represents a vector of the three-dimensional model of scalar Q^{-1} values. The Laplacian smoothing is introduced to prevent noisy data from producing unstable solutions with large variance. This is different from the standard Levenburg-Marquardt approach in that it constrains neighboring blocks to be close to one another. Furthermore, since negative attenuation is physically unrealistic inversion models were required to have non-negative Q^{-1} values. The matrix system in equation (4) is solved via a conjugate gradient algorithm called LSQR [*Paige and Saunders*, 1982; *Spakman and Nolet*, 1988].

There is considerable variability in the data. Box plots of the original t^* and f_c values for each station are presented together in Figures 4a and 4b. Box plots, like histograms, summarize the distribution of the values on a per station basis. Median, interfourth quartiles, octiles, and outlier values are conveniently shown on the same plot for comparison. The t^* estimates vary from negative values to several very large outliers. The f_c similarly vary widely, up to 80 Hz in some instances. Since there
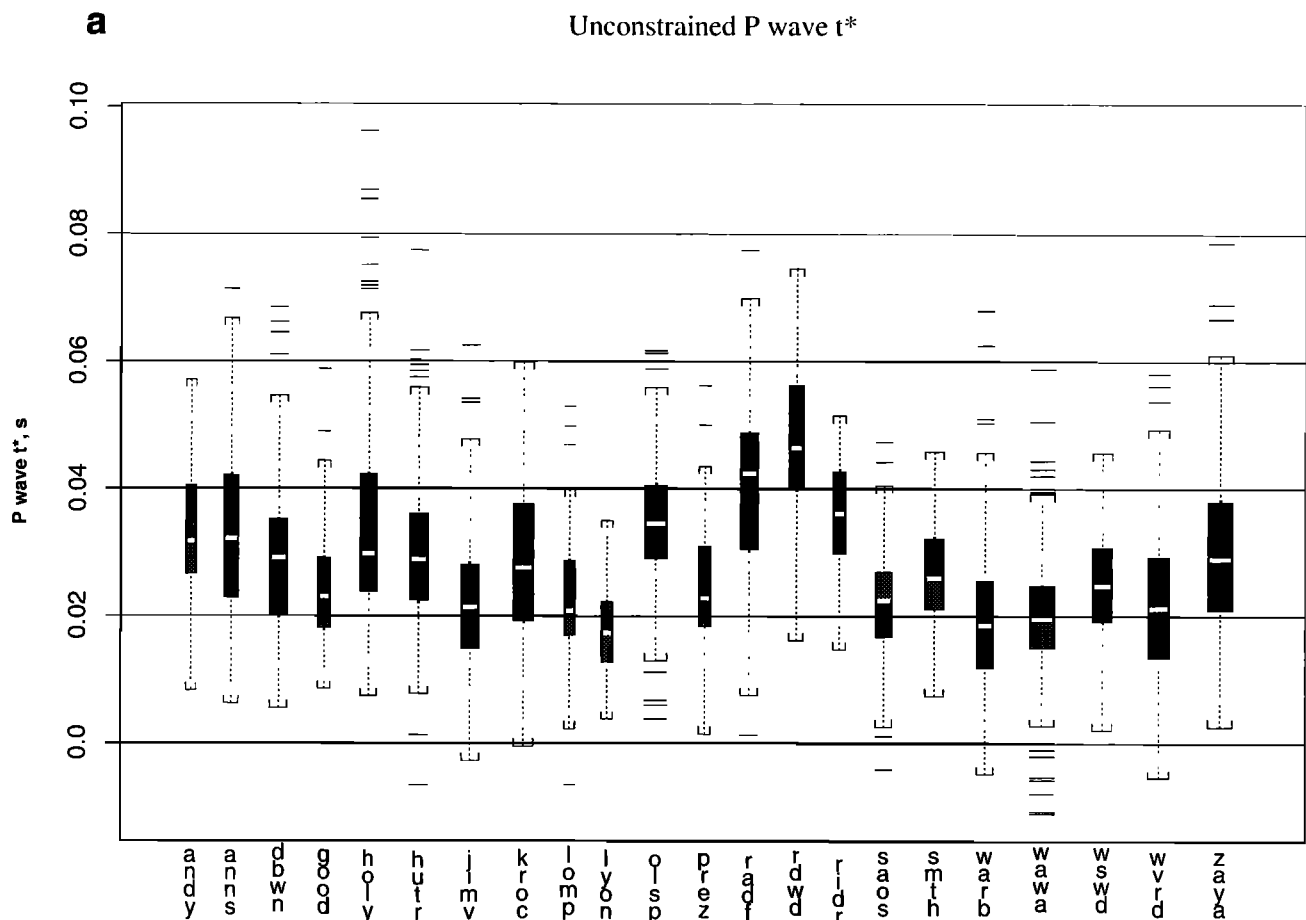

Figure 4. Box plots of the unconstrained t^* values for full data set for (a) P wave t^* and (b) S wave t^*. Box plots show, for each station, the distribution of the t^* median (horizontal white bar in each dark rectangle), interfourth quartiles (bounded by dark rectangles), octiles (bounded by dashed lines and brackets), and outliers (horizontal dark lines). The width of each box plot is proportional to the number of data for each station.
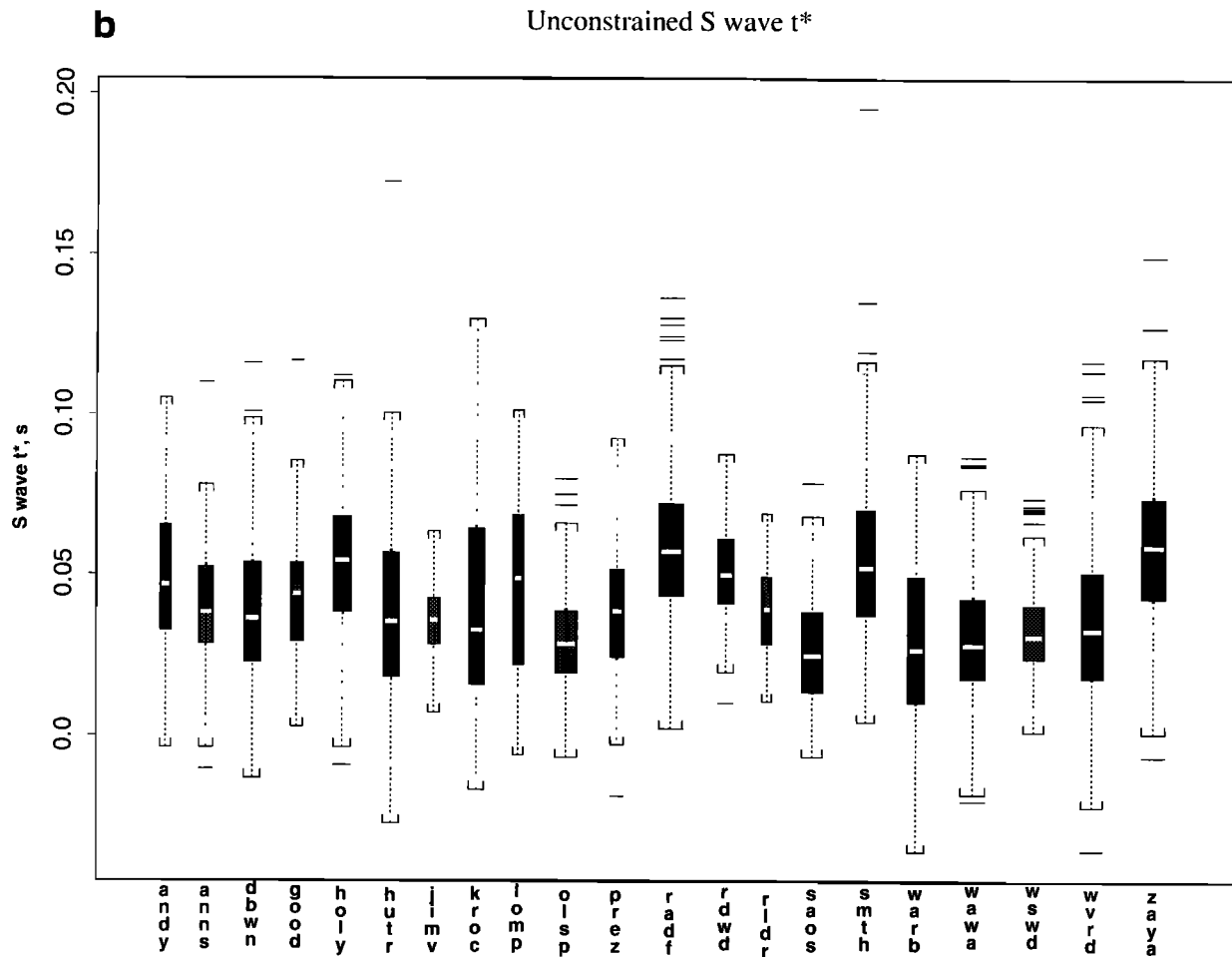
b Unconstrained S wave t*

Fig. 4 (continued)

is a trade-off of t* and f_c, we are concerned about possible systematic correlations between these parameters. Contours of median t* and f_c values for each station indicate that there is no apparent spatial correlation between the overall summaries of the two parameters for each station. Plots of the contoured median t* values show a general high in the southwest part of the target area associated with stations radf, rdwd, olsp, ridr, and zaya (Figure 5a). Corresponding contour plots of median f_c do not correlate at all with the t* surface. The contour plots of median t* do correlate with site geology. Sites located on the Franciscan assemblage generally have low attenuation (sites jimv, warb, saos, and wvrd). The other sites are located on younger Cenozoic sedimentary rocks and generally have greater t* values. A more detailed discussion of the interplay of site effects with site geology for this data set is given by *Lindley and Archuleta* [1992].

To assess if the variability of the t* values could be reduced by removing some of the trade-off of t* with f_c, all events that were recorded at four or more stations were selected for a second analysis. In this second analysis, the corner frequency was constrained to have the same value for recordings of the same event at different sites. A joint inversion of the spectra for each event was determined with t_0^* and Ω_0 allowed to vary for each spectrum and the corner frequency constrained to a single value. The t* estimates calculated in this manner had similar distributions as those calculated in the unconstrained case except the interfourth quartile distances were smaller (Figure 6 and

Figure 7). This implies that the new data set had less variability than the unconstrained case. The main difference in the median values was at stations holy, prez, and anns, which have higher median values than in the unconstrained case (Figures 5a and 5b). The corner frequencies calculated in this manner have much less variability than before. Box plots of f_c for the constrained P wave determinations are presented in Figure 8. The data distributions in the box plots indicate that t* estimates greater than 0.07 and less than 0.0 are outliers. To insure robustness in the inversion, all t* data beyond these limits were eliminated. The S wave data were considerably sparser than the P wave data, with fewer events recording at several stations simultaneously. Because of this we chose not to constrain the S wave spectral estimates, so the data, as presented in Figure 4b were used as is with t* estimates greater than 0.07 and less than 0.0 removed as in the P wave data. We found no special correlation of average f_c to t* determinations in the S wave data; for completeness we present box plots of the S wave f_c values in Figure 8b. The final data set included 2442 (constrained) P wave and 2115 (unconstrained) S wave t* estimates.

Results

Tomographic inversion results are presented in Figures 9-14 as gray shades of Q_p^{-1} and Q_s^{-1}, respectively. Since there is no satisfactory quantitative method for choosing λ, several choices
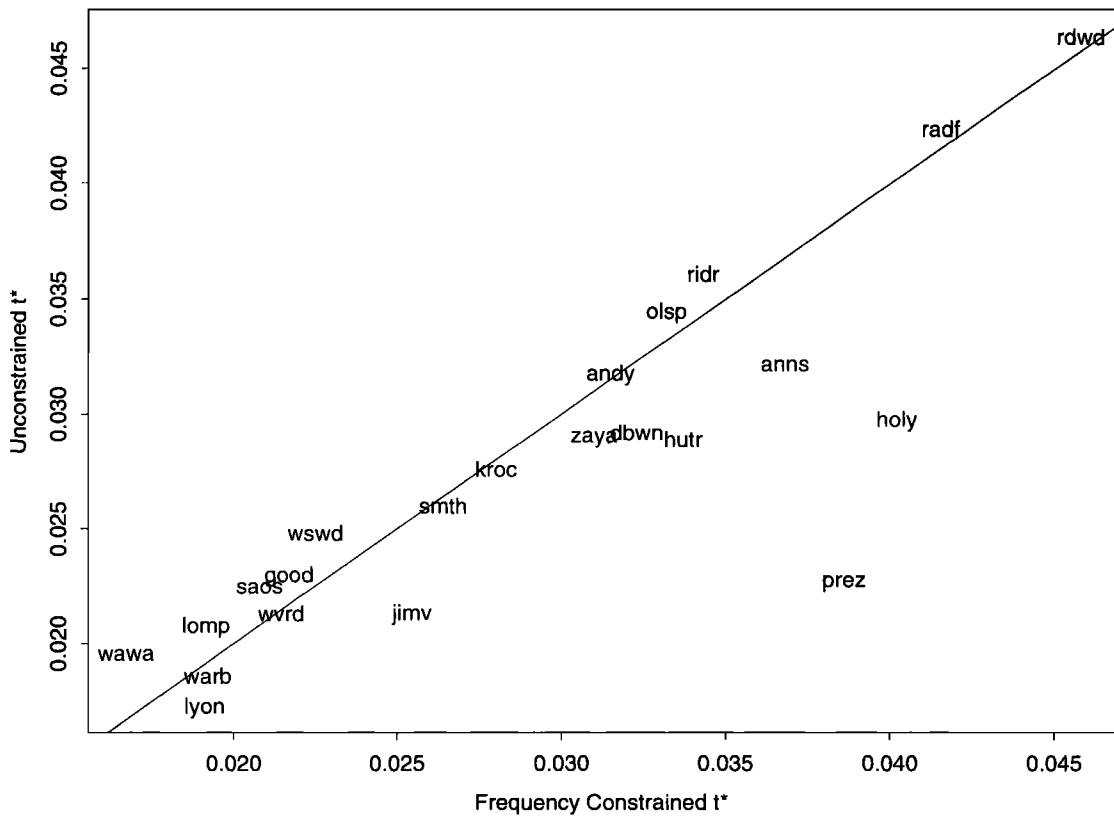
Comparison of t* estimates

Figure 5. Comparison of t* values for estimates using f_c constraints versus unconstrained determinations. Notice that stations anns, holy, prez, and jimv appear to be considerably larger for the constrained estimation.
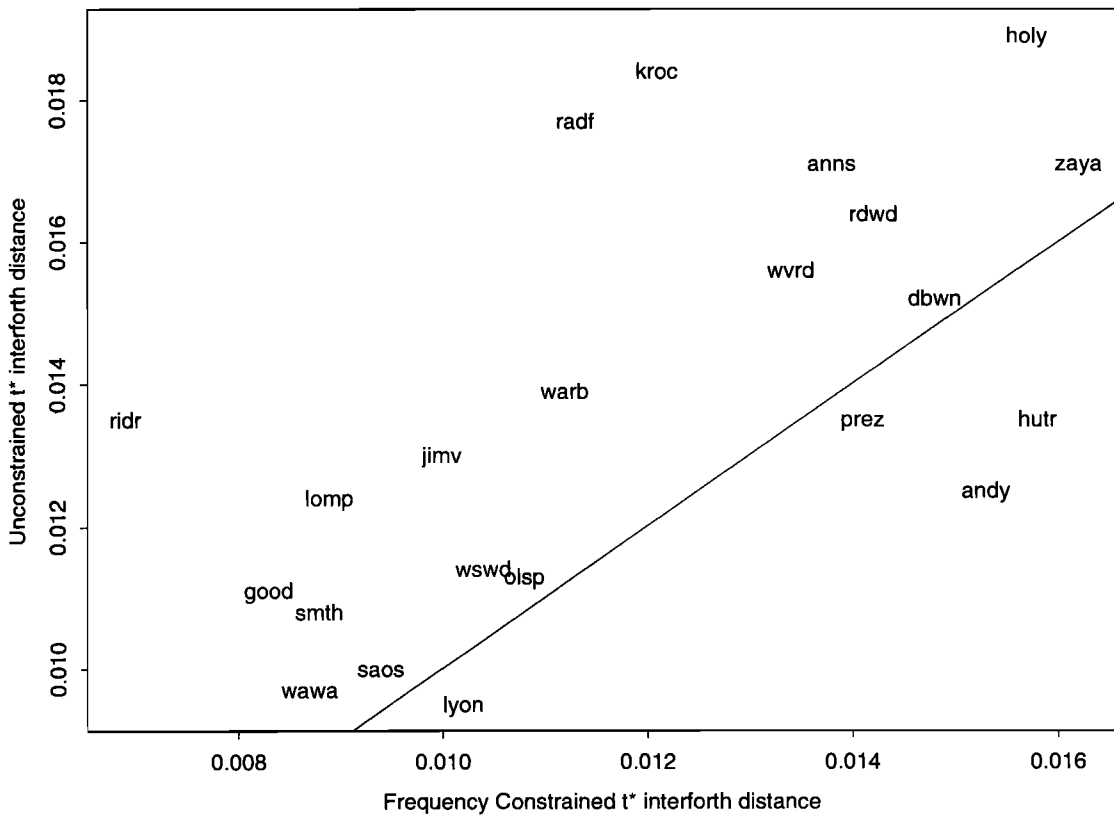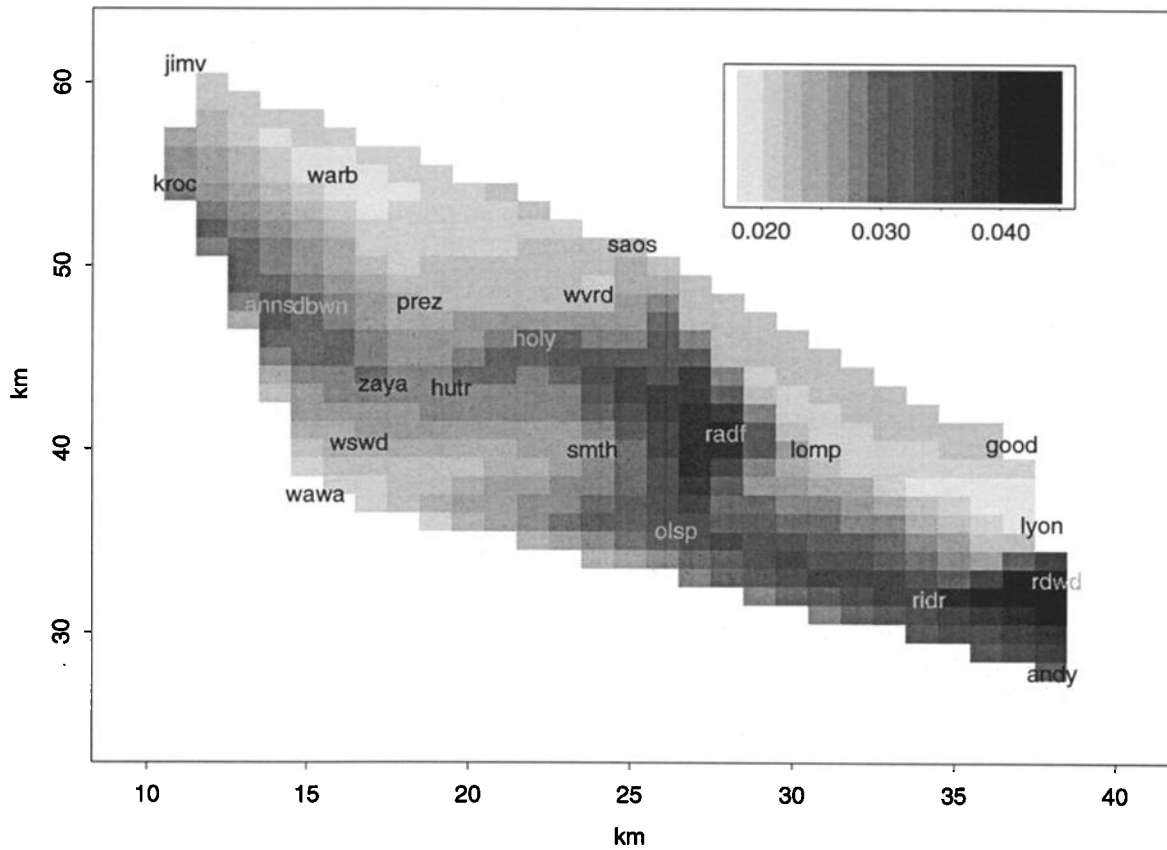
Comparison of Quartile distances

Figure 6. Comparison of the data spread, approximated by the interfourth quartiles, between constrained and unconstrained estimates of t*. Notice that the data are considerably more spread out in the unconstrained versus the constrained estimates.
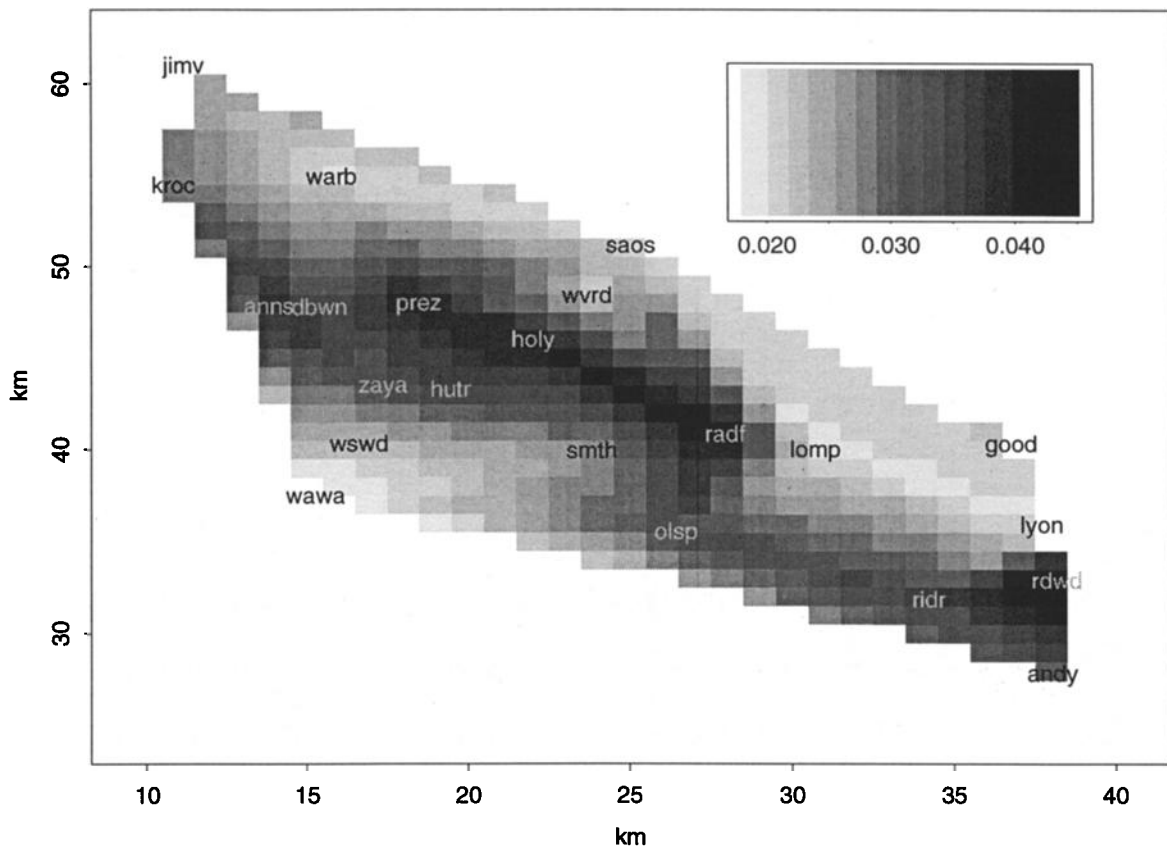
Figure 7. Contour plots of the median t* values: (a) unconstrained inversions and (b) constrained estimates. Median values were spatially interpolated for each data set. The main difference in the median values lies near the stations which exhibited significant changes shown in Figure 4.
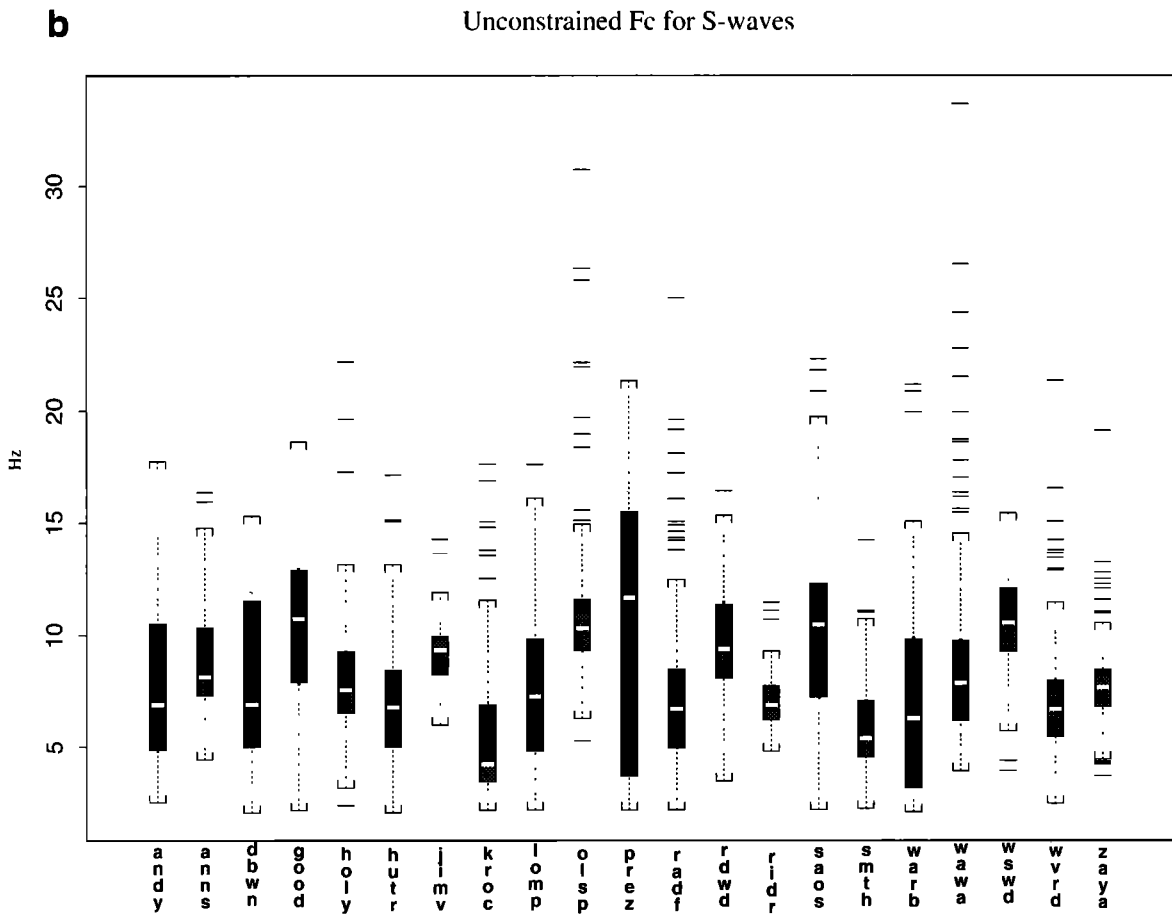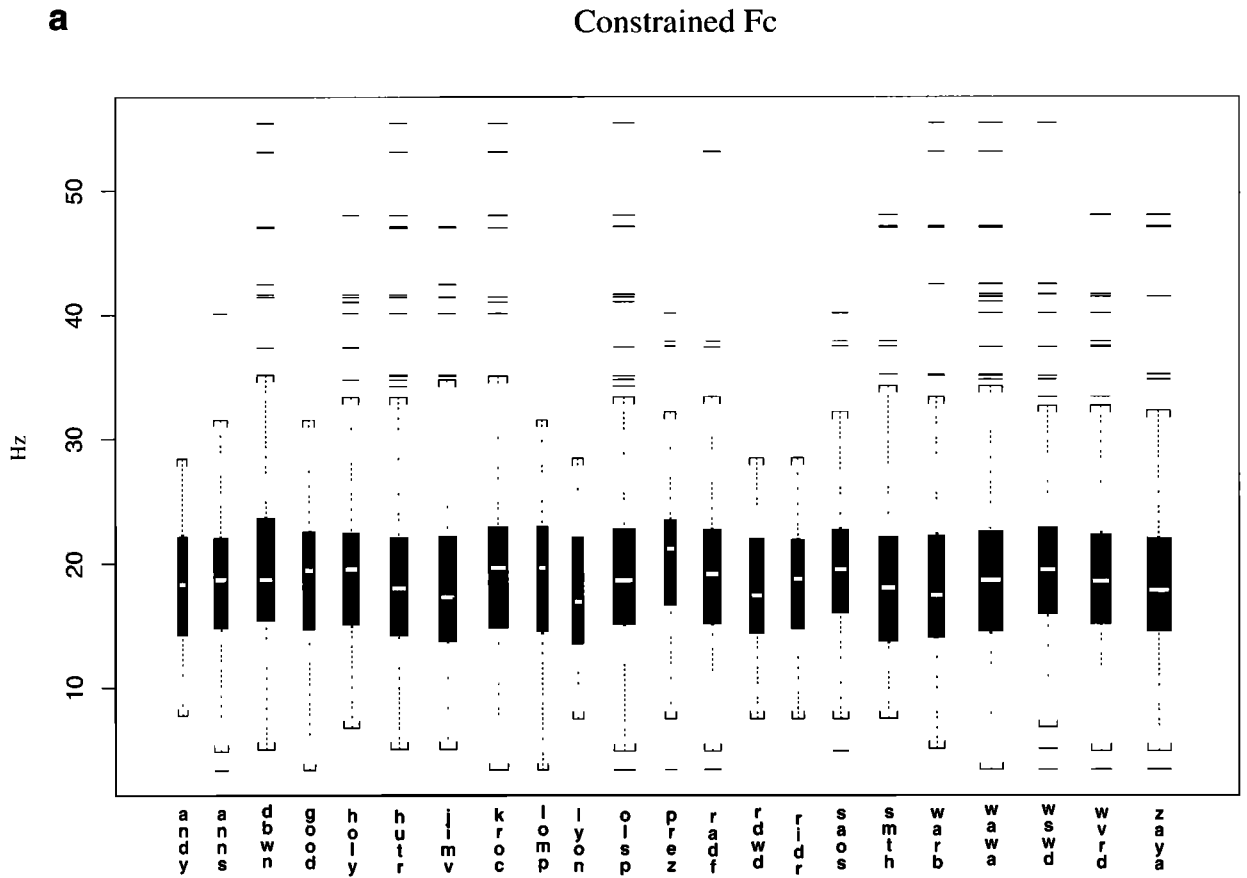
a Constrained Fc

b Unconstrained Fc for S-waves

Figure 8. a) Boxplot of the f_c values accumulated for P wave spectra (see fig. 4a for details). b) Corresponding plot for S wave determinations.
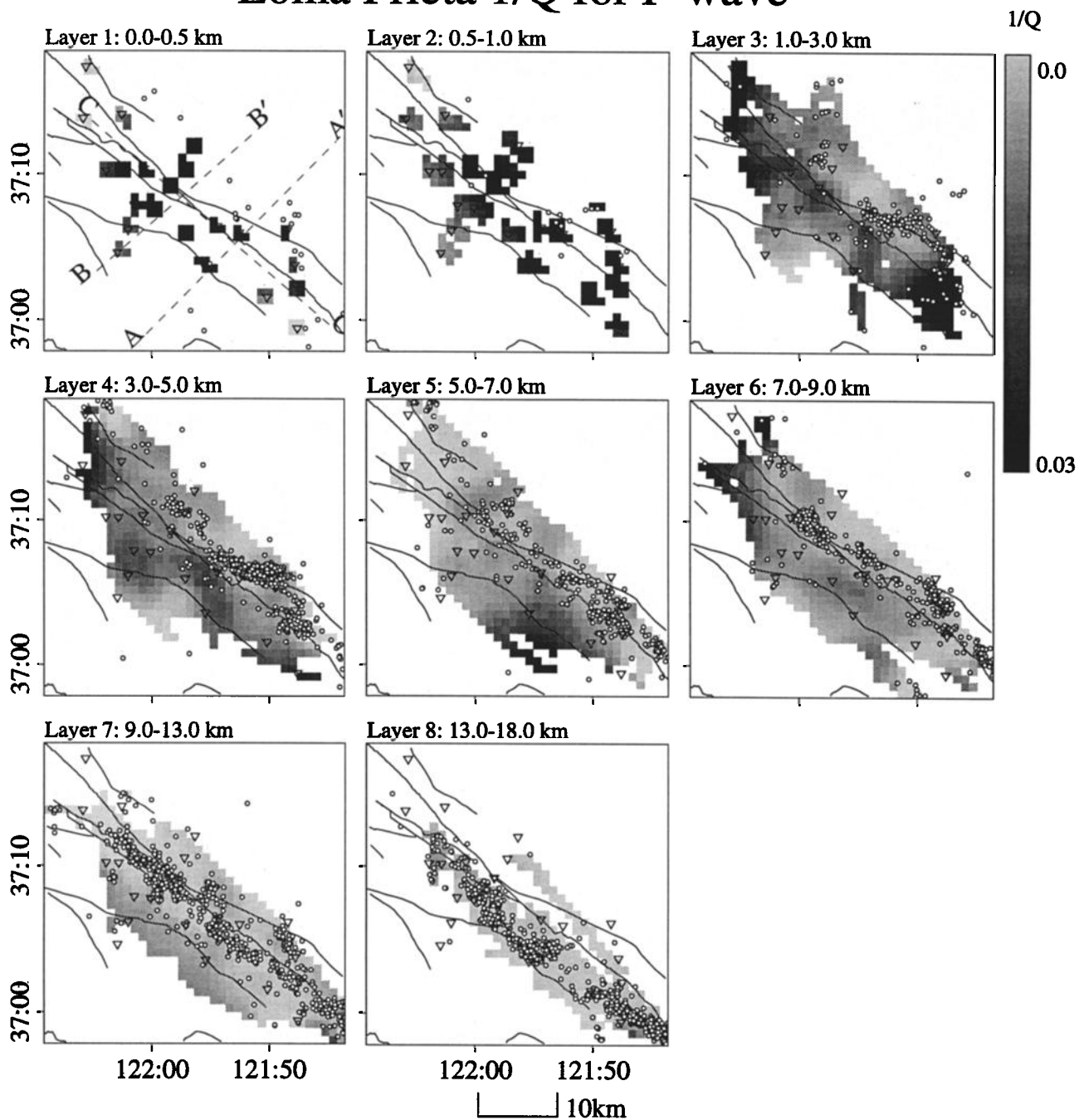
Loma Prieta 1/Q for P-wave

Figure 9. Three-dimensional tomographic inversion for Q^{-1} using P wave t* estimates.

of λ were tested and the one that provided a reasonable trade-off of residual reduction to model smoothness is presented here ($\lambda = 1$ for Q_p and $\lambda = 0.9$ for Q_s). We were interested primarily in structural features of wavelength approaching that of the velocity inversion.

Near the surface (to 1 km depth) the incident rays are nearly vertical, so ray paths and anomalies are concentrated around the stations (Figure 9a). The predominant near-surface signal is high attenuation in the vicinity of the stations. The high attenuation region correlates with a low velocity anomaly extending 5-7 km

depth that was previously interpreted as a sedimentary basin situated between the San Andreas and Zayante faults. The relatively high attenuation extends to layer 6 (7-9 km depth) southwest of the San Andreas fault near the center of the target region. A close-up view of the deeper layers is provided in Figure 10 where the correlations of Q_p and seismicity are clarified. This trend is observed on vertical cross sections of the model in Figure 11. Sections AA' and BB' are perpendicular to the San Andreas fault and show the high attenuation in the hanging wall of the fault. The fault zone, as defined by the
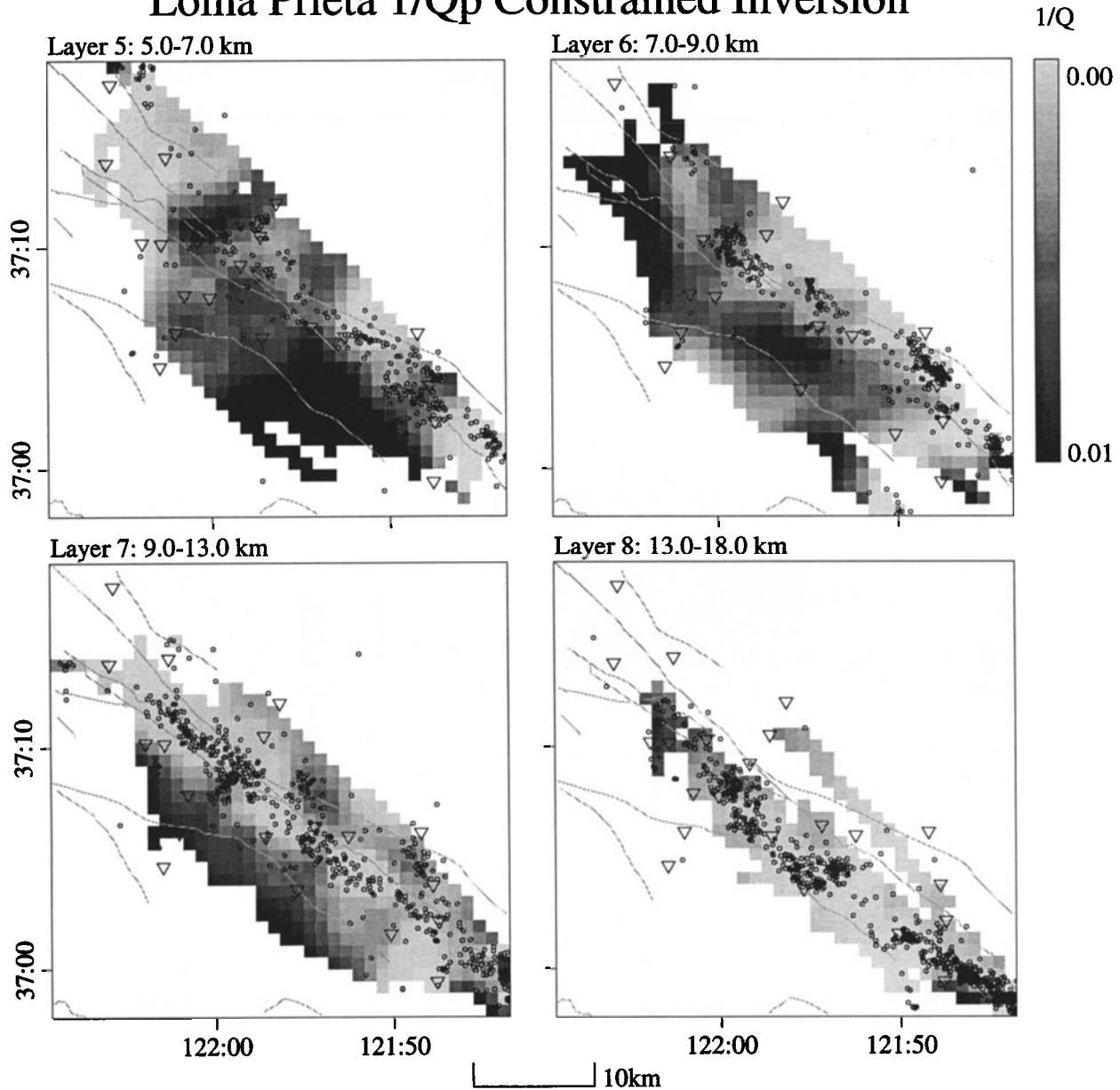
Loma Prieta 1/Qp Constrained Inversion

1/Q

Layer 5: 5.0-7.0 km

Layer 6: 7.0-9.0 km

0.00

0.01

Layer 7: 9.0-13.0 km

Layer 8: 13.0-18.0 km

122:00   121:50

122:00   121:50

10km

Figure 10. Close up of layers 5-8 of Figure 9 plotted with a more condensed scale.

spatial distribution of hypocenters, does not appear to have high attenuation. Section CC', which parallels the San Andreas, shows a distinct decrease of attenuation with depth.

The S wave attenuation inversion exhibits a pattern similar to the P wave (Figures 12, 13 and 14). High attenuation is prevalent southwest of the surface trace of the San Andreas fault down to 9.0 km depth. In layer 8 (13-18 km depth) two small high attenuation patches are observed. The S wave data set is smaller than the P wave data set, and the variations of t* estimates are more variable. Attenuation anomalies subsequently have more variance. Compare layer 5 (Figure 13a) of the S wave inversion with the corresponding layer of the P wave analysis (Figure 10a). While the S wave inversion appears to show more extreme variation, the overall pattern described above for the Q_p inversion

is evident in the S wave result: the hanging wall of the fault zone has an apparent high attenuation. In the Q_S inversion, though, we observe a slightly higher attenuation in the fault zone (Figures 13c and 13d), as determined by the seismicity (cross sections A-A´ and B-B´ in Figure 14). This is opposite the pattern seen in the Q_p (cross sections A-A´ and B-B´ in Figure 11).

In Figure 15 we provide a first order estimate for the ratio of Q_p to Q_S. We feel that because of the variability of the results, a formal, quantitative analysis of the Q_p/Q_S ratio is not entirely appropriate, and we refrain from interpreting these values in detail. We note, however, that there appears to be a significant pattern of exceptionally high Q_p/Q_S ratio in the deep portion of the model (layers 6-8, 7-18 km depth, Figure 15f - 15h) where the ratio exceeds a factor of 10.
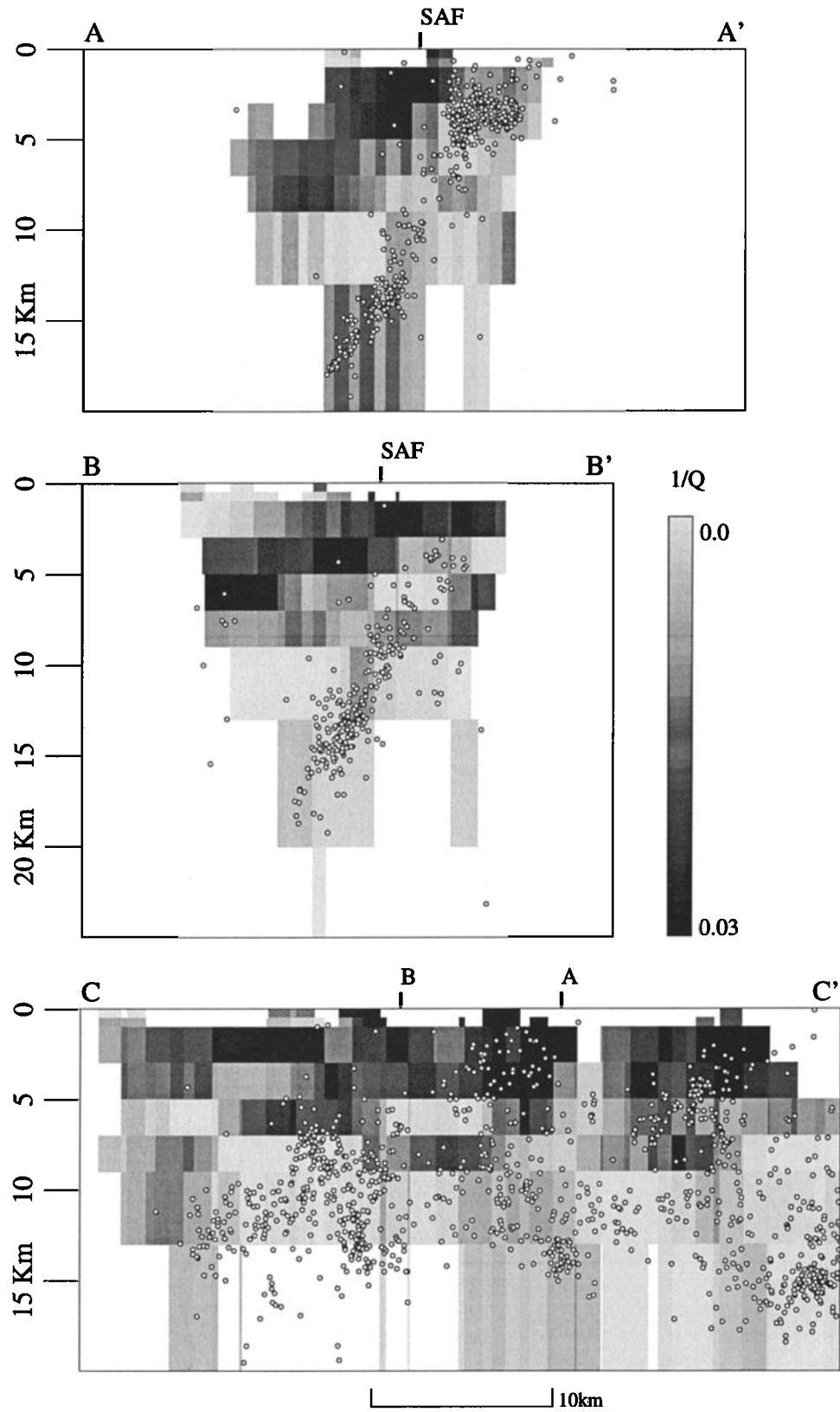
Figure 11. Vertical cross section of three-dimensional inversion in Figure 8 (a) perpendicular to San Andreas fault, central, (b) perpendicular to San Andreas fault to the south and (c) parallel to San Andreas fault. A plan view of the cross sections is presented in Figure 1.
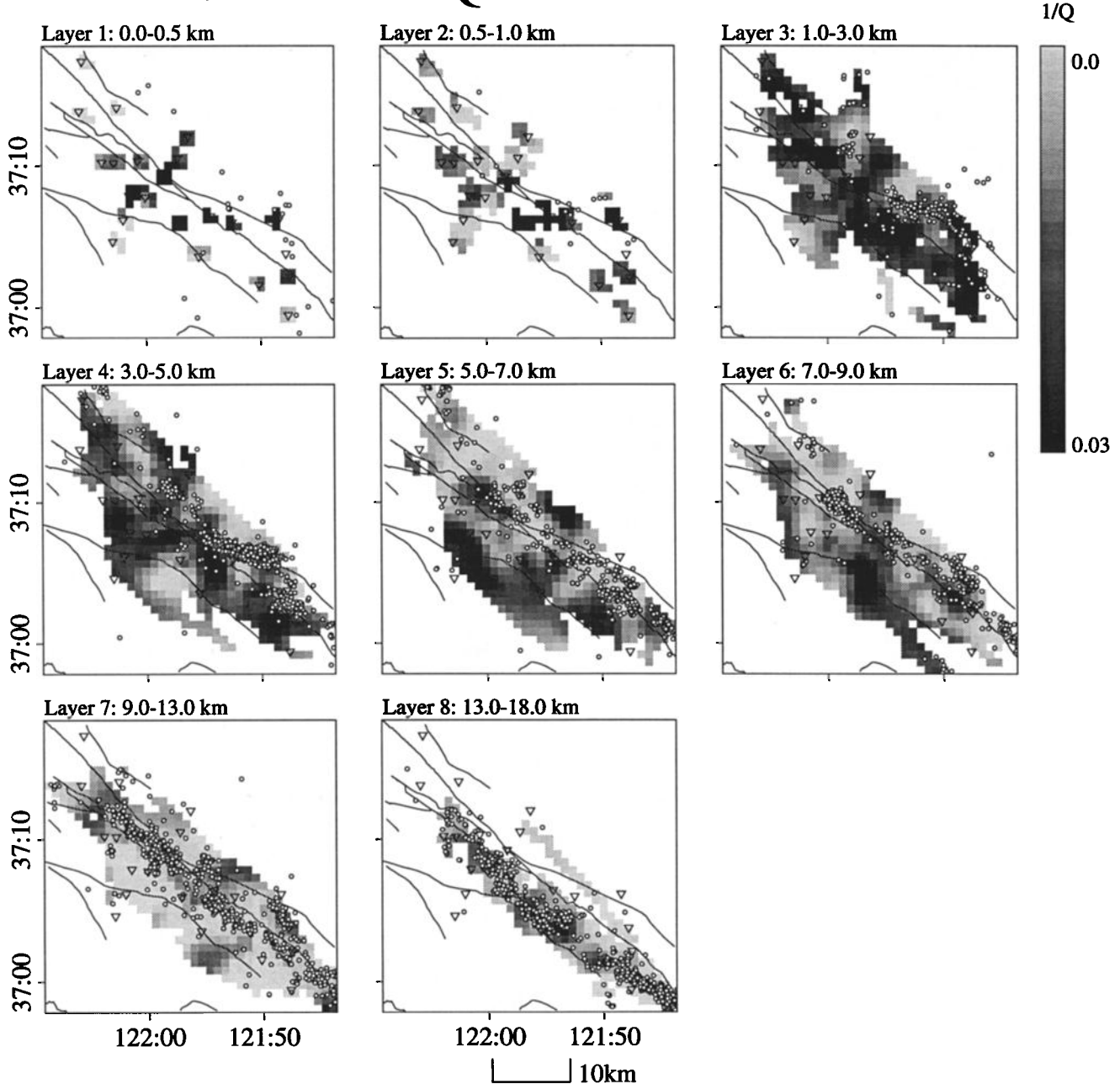
Loma Prieta 1/Q inversion for S-wave

Figure 12. Three-dimensional tomographic inversion for Q^{-1} using S wave t* estimates.

Resolution Analysis: Error Bars

To estimate the effect of variable data on the results we used a subsampling technique called the Jackknife [*Efron*, 1982; *Lees and Crosson*, 1989; *Tichelaar and Ruff*, 1989]. The jackknife provides an estimate of the variance of the models based on the influence samples of the data set have on the model. The data are divided into 30 nonoverlapping sets, and inversions are derived for each set. The statistical summaries of the set of models provide an estimate of the variance of the inversion model. These estimates are most reliable near the center of the model where data density is high. The error estimates for the center of the models are small, as shown in Figures 16a and 16b. Near the edges of the model the jackknife errors indicate unreliable model

estimates, although these parameters are also poorly resolved because of reduced sampling of seismic waves in these regions. We therefore discount the model near the edges.

Spatial resolution is usually estimated by calculating point spread function for regions of interest and examining hit count displays showing the distribution of the data (Figure 17). Where the data distribution is very dense, as in the center of the model where, typically, 100 rays penetrate individual blocks, the resolution is excellent. Point spread functions near the center of the model indicate that we can resolve features that are 2-3 blocks, or 3 km in length. Near the edges of the model smearing degrades spatial resolution considerably and localized anomalous features are not reliable estimates of Q for those blocks. Poorly sampled blocks can have as few as one ray penetrating and
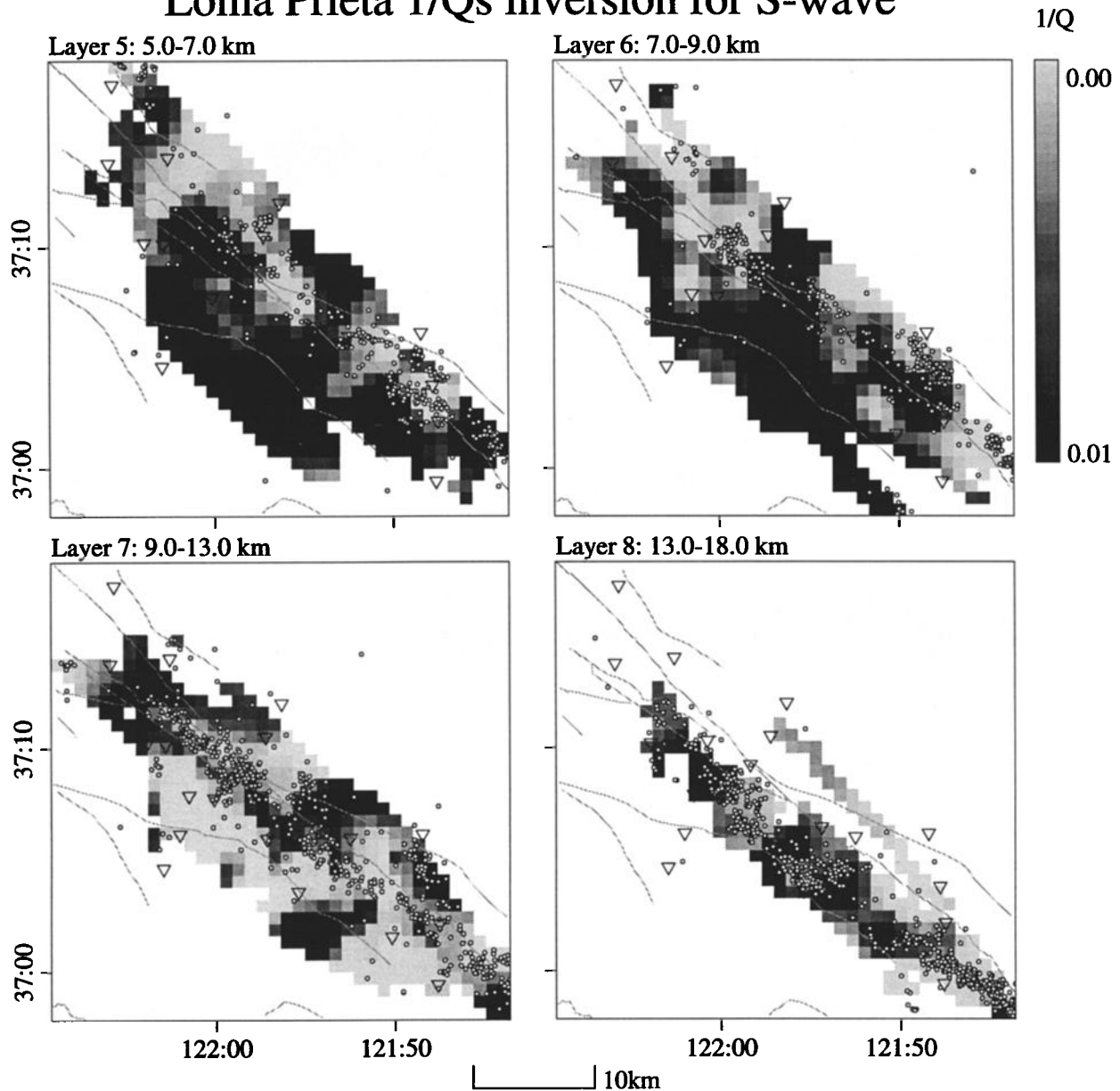
Loma Prieta 1/Qs inversion for S-wave

Figure 13. Close up of layers 5-8 of Figure 12 plotted with a more condensed scale.

tomographic methods do not provide reliable results in this situation (Figure 17). We therefore restrict our interpretation to features located in the heavily sampled regions near the center and we consider only broad features for interpretation. The smoothing, applied by the Laplacian constraint, insures that extreme variations between blocks are avoided and most of the features have considerable continuity.

One concern that arises in a study of attenuation is the effect of anomalous site response near the surface. We have investigated this effect by examining resolution kernels directly below stations. We found that anomalous attenuation leaked into the subsurface layers only down to 2-3 km depth in the worst case and less than 1 km is several locations. The large number of crossing rays beneath stations suppresses smearing of anomalous site effects into the deeper parts of the model.

There are several possible sources of error that we have not accounted for and that should be pointed out as caveats to this analysis. (1) There is an inherent bias due to the initial assumption about the form of the (Brune) spectral model. If indeed it is wrong to assume the simple parametric description of the source spectrum that we used, then this would represent a systematic bias which is not included in the analysis. (2) There is a bias due to possible errors in the assumed velocity model. This error is greatest for the S wave inversion, where V_s was derived from V_p scaled by $3^{1/2}$. The Vp estimates are derived from a much larger data set than that included in this study, and the velocity model has been studied in greater detail. We are thus confident that errors introduced by the velocity model are small. (3) The trade-off of f_c and t* presents a difficult problem which we have attempted to reduce by constraining the f_c values for
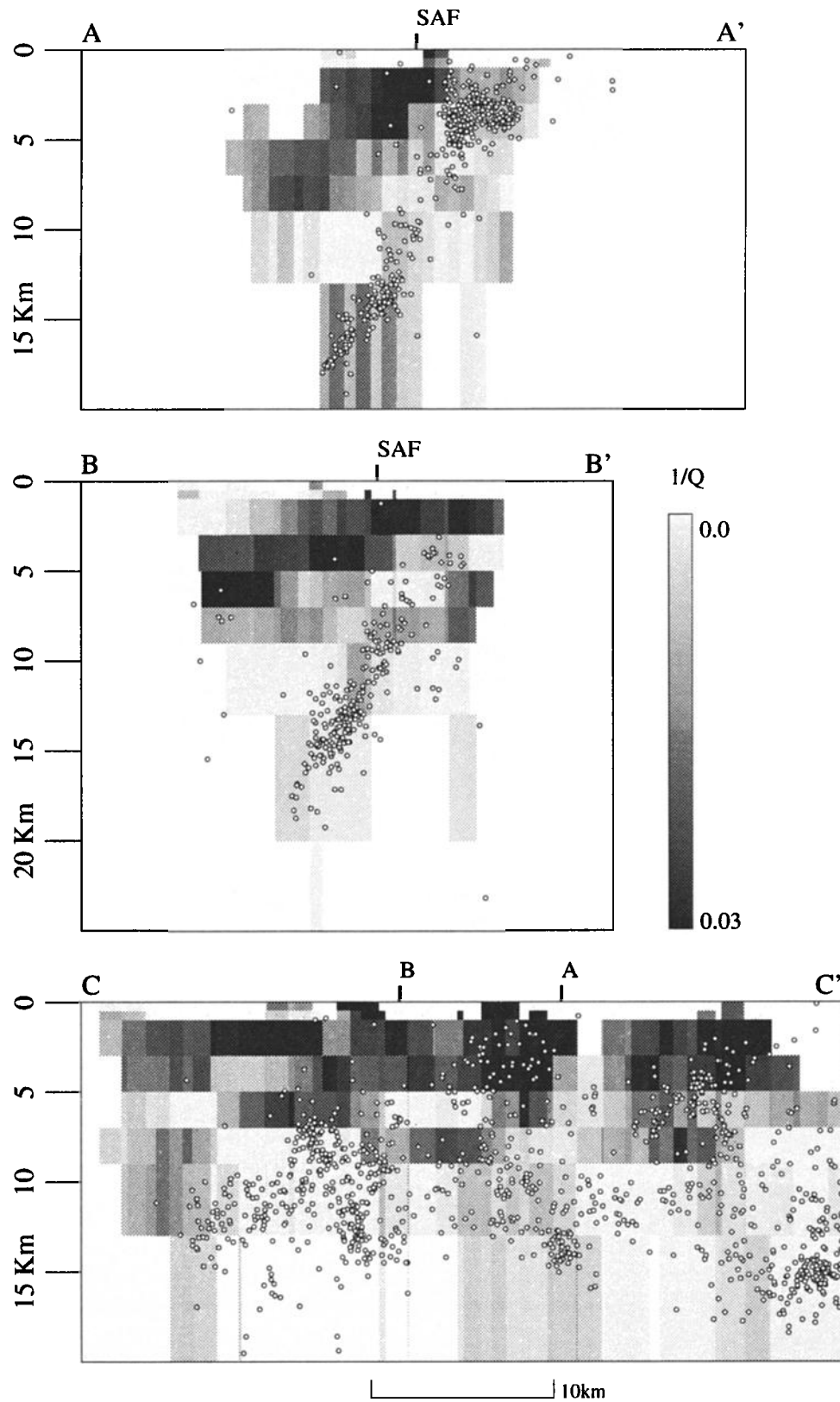
Figure 14. Vertical cross section of three-dimensional inversion in Figure 10 (a) perpendicular to San Andreas fault, central, (b) perpendicular to San Andreas fault to the south, and (c) parallel to San Andreas fault.
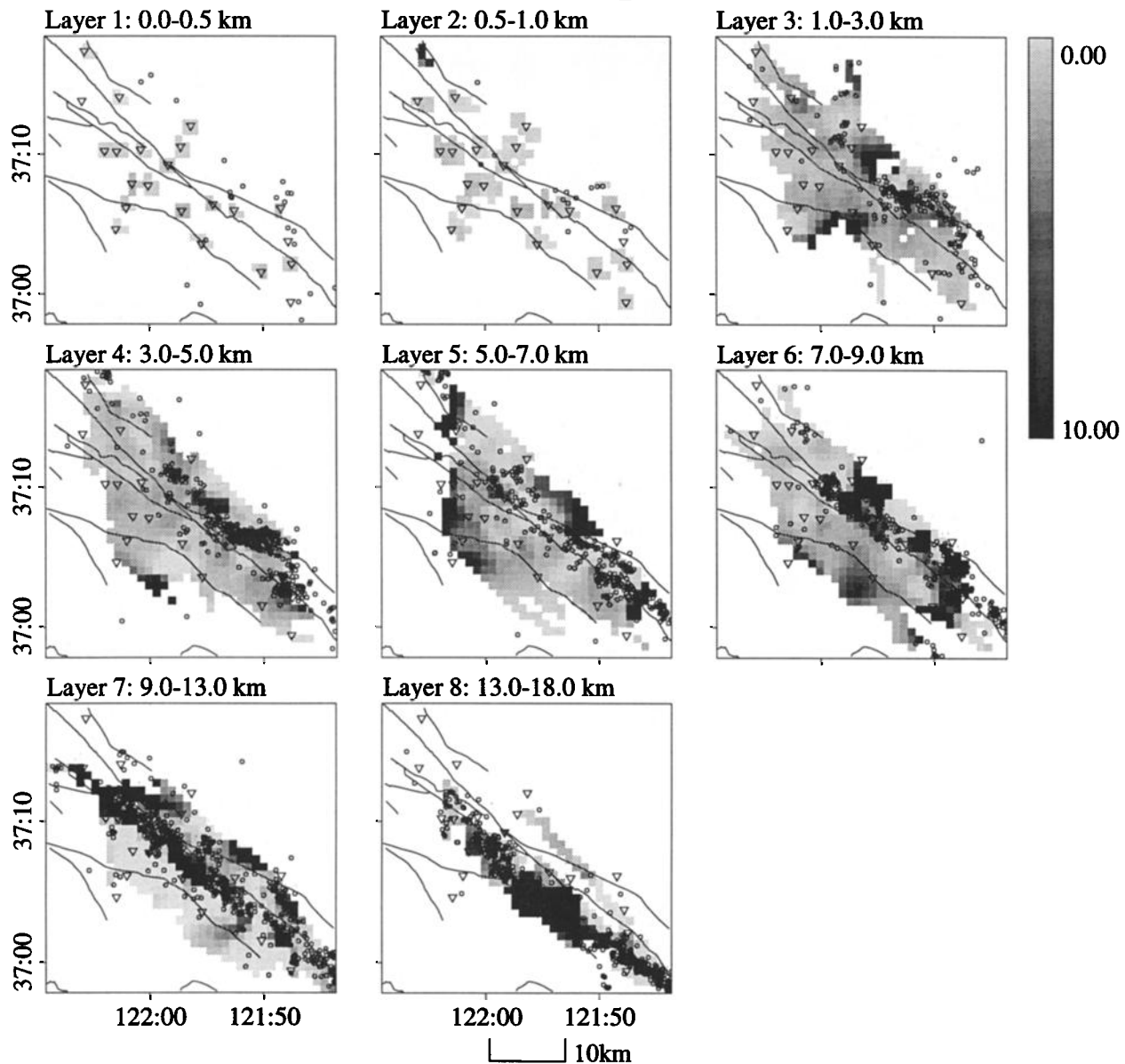
Loma Prieta Qp/Qs

Layer 1: 0.0-0.5 km   Layer 2: 0.5-1.0 km   Layer 3: 1.0-3.0 km

Layer 4: 3.0-5.0 km   Layer 5: 5.0-7.0 km   Layer 6: 7.0-9.0 km

Layer 7: 9.0-13.0 km   Layer 8: 13.0-18.0 km

Figure 15. Q_P/Q_S ratio calculated by block-wise division of results presented in Figures 9 and 12.

common event data, however, there remains the possibility that some of the spectral fit associated with t* is included in f_c and vice versa. We do not, at this point, have a completely satisfactory answer to this question. (4) We have stated above that the attenuation includes all effects of waveform distortion along the raypath. We have not compensated the spectra for focusing effects due to high-velocity gradients in the model. Indeed, our velocity model is smoothed such that large gradients are suppressed, and we have no a priori information to support the level of smoothing we have chosen. This means we cannot attribute all the residual t* to intrinsic attenuation. (5) We have not explicitly accounted for source radiation effects. It is theoretically possible that the source radiation pattern or directivity of rupture could effect measurements of the corner frequency and t*. However, because the constrained fits had smaller variations in measurements of t*, it appears that

azimuthal source effects are not the primary source of error in the measurement of t*. In light of these considerations, and because the level of regularization plays an important role in the variance of perturbations in inversions of this sort [Lees and Shalev, 1992], we feel it is misleading to interpret exact derived values of Q in our model. We expect that the sense of the perturbations, on the other hand, and the structural features discussed below are robust and deserve careful consideration.

Discussion

The main results of this paper can be summarized in three observations: 1) There is a strong pattern of low Q in the upper 1-3 km of the P and upper 5-7 km of the S wave inversions, observed primarily to the southwest of the San Andreas fault.
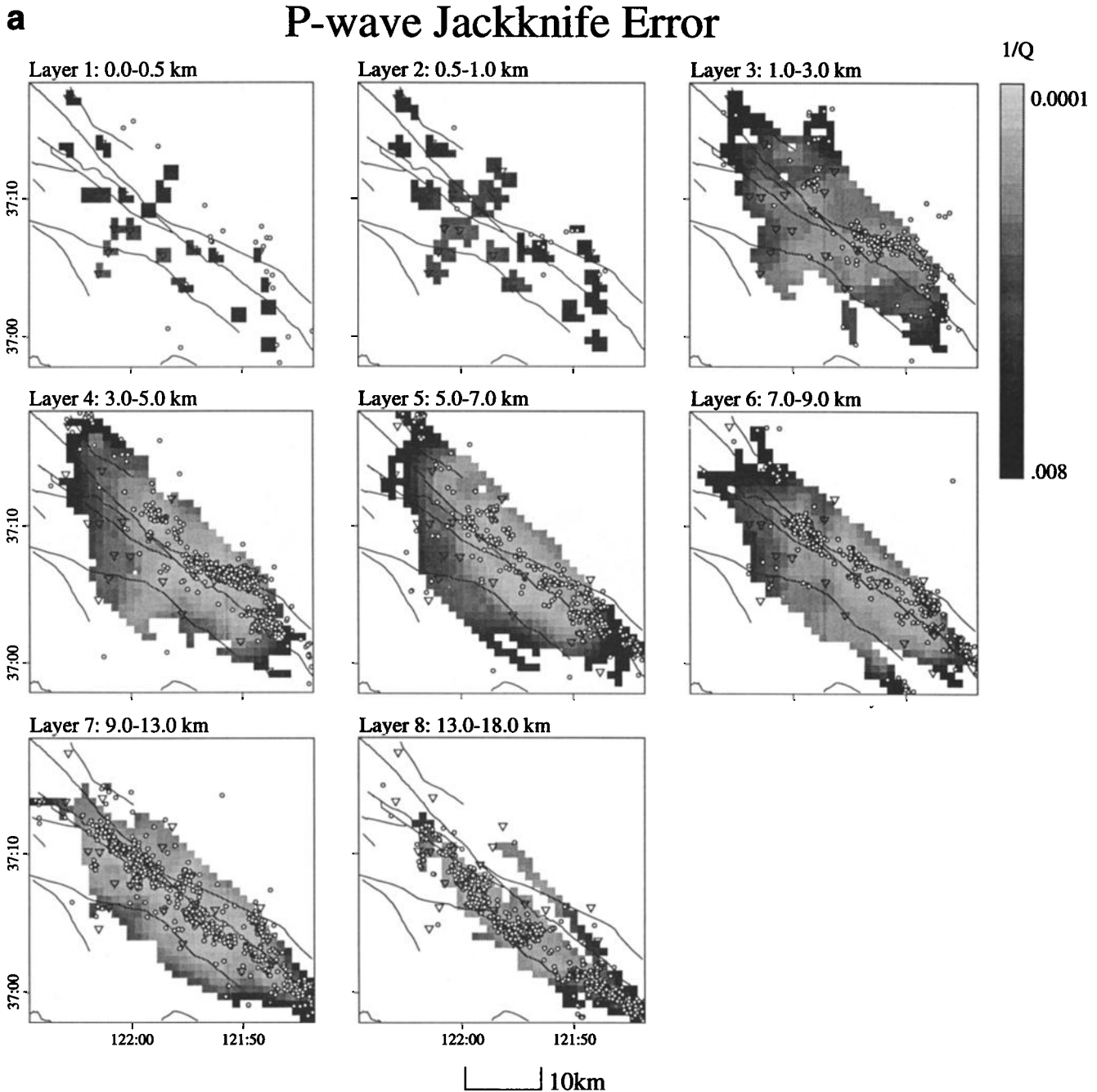
Figure 16. Jackknife estimates of model errors: (a) Q_p^{-1}. (b) Q_s^{-1}.

This trend is more prominent for the S waves in the Salinian rocks south of the surface trace of the San Andreas fault. 2) There is an apparent high Q_p dipping along the observed, seismically defined, fault zone (see cross sections A-A′ and B-B′ of Figure 11). 3) There is an apparent low Q_s extending along the seismic zone near the hypocenter of the Loma Prieta mainshock (layers 7 and 8). We expect that differential attenuation is due to a number of competing factors, including variations in lithology and rock type, crack distribution, pore fluids, pore fluid saturation levels, and confining pressures.

The high near-surface attenuation is observed along a marine sedimentary basin spanning the region between the Sargent and Zayante faults. This apparent wedge of low-Q material correlates with a low velocity body estimated for this region by travel-time tomography [*Eberhart-Phillips et al.*, 1990; *Eberhart-Phillips and Stuart*, 1992; *Lees*, 1990; *Lees and Shalev*, 1992; *Shalev and Lees*, 1994] and seismic refraction data [*Mooney and Colburn*, 1985]. These also correlate with a region of high V_p/V_s ratio [*Thurber and Atre*, 1993]. As expected, Q_p and Q_s generally increase with depth to about 20 km. There is an apparent step increase (Figures 11 and 14) of Q in the vicinity of 10 km depth along the San Andreas fault, which has been previously observed as being a major seismic boundary between higher V_p/V_s versus lower V_p/V_s [*Fuis and Mooney*, 1990; *Thurber and Atre*, 1993].

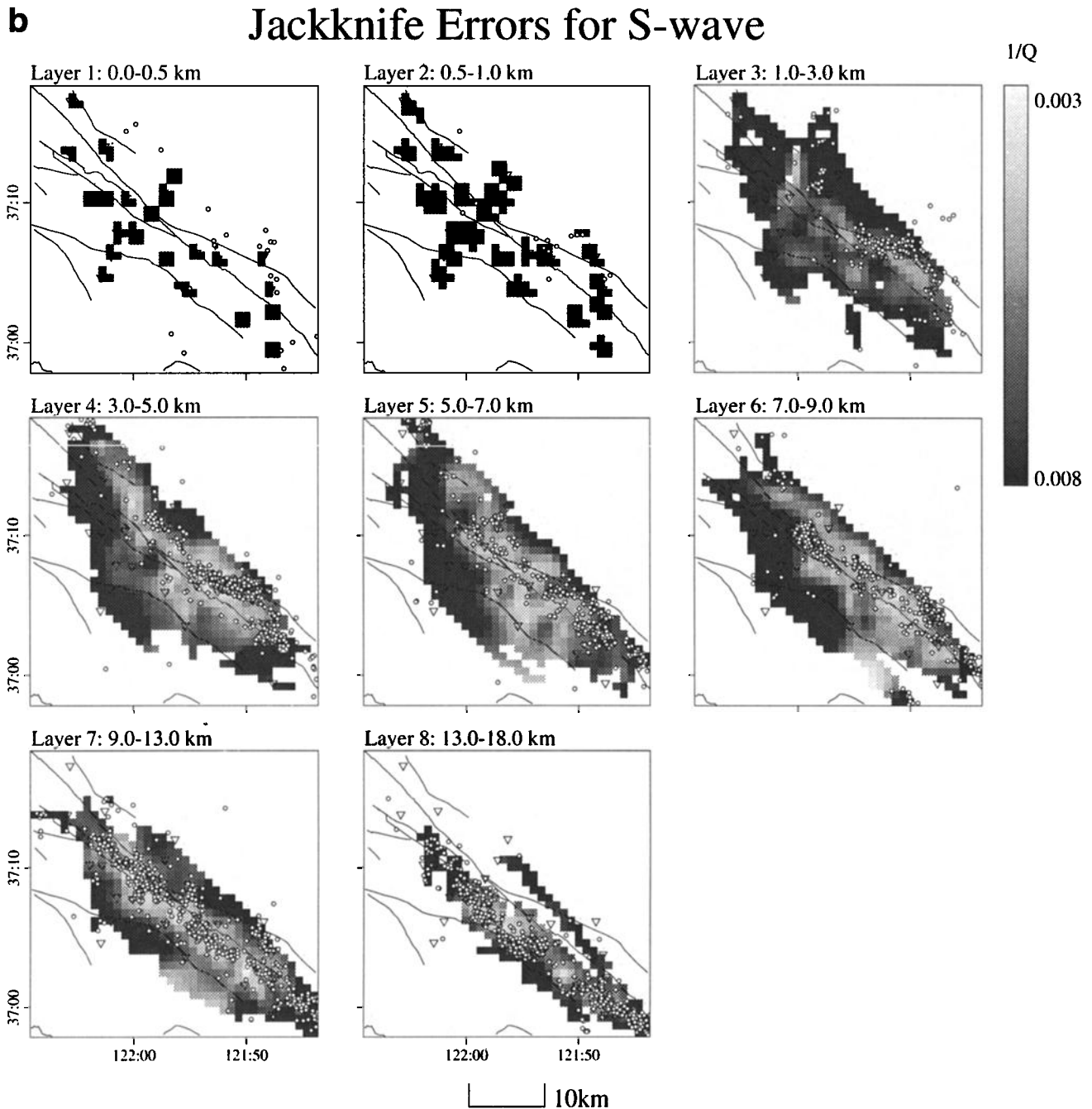**b**   # Jackknife Errors for S-wave

Figure 16. (continued)

The exception to the general increasing trend is in the deep fault zone (9-18 km depth), dipping to the southwest, which is characterized by relatively high Q_p/low Q_s and also has corresponding high P wave velocities. The values of Q_p/Q_s in this region are significantly greater than 10. Layers 3, 4, 6, 7, and 8 all show anomalously high Q_p/Q_s in the fault zone region. (Layer 5 exhibits only moderate values of Q_p/Q_s in the fault zone with high values of Q_p/Q_s near the edge of the well resolved regions. Layers 3, 6 and 7 also include patches, near the edge of the model, where high Q_p/Q_s is observed.) Laboratory measurements suggest that partially saturated rocks have $Q_p/Q_s <$ 1, where as fully saturated material exhibits $Q_p/Q_s > 1$ [*Winkler*

and Nur, 1979]. If the Q observed in this study is due to porous saturation, we would speculate that the rocks along the fault zone are fully saturated since in our case, along the deep portion of the fault zone, $Q_p/Q_s > 1$. This, in itself, is not surprising considering the depth range of 7-12 km. We note that our results differ from those of *Wittlinger et al.* [1983] in that we observed a high Q_p in the fault zone as opposed to their lower Q_p. We suspect that their much lower resolution study most likely mapped lower Q_p from shallow sedimentary regions into the fault zones they observed. The slightly lower Q_s observed in our study suggests that there is some attenuation effect contributing to waveform distortion from the fault zone. We have assumed, of
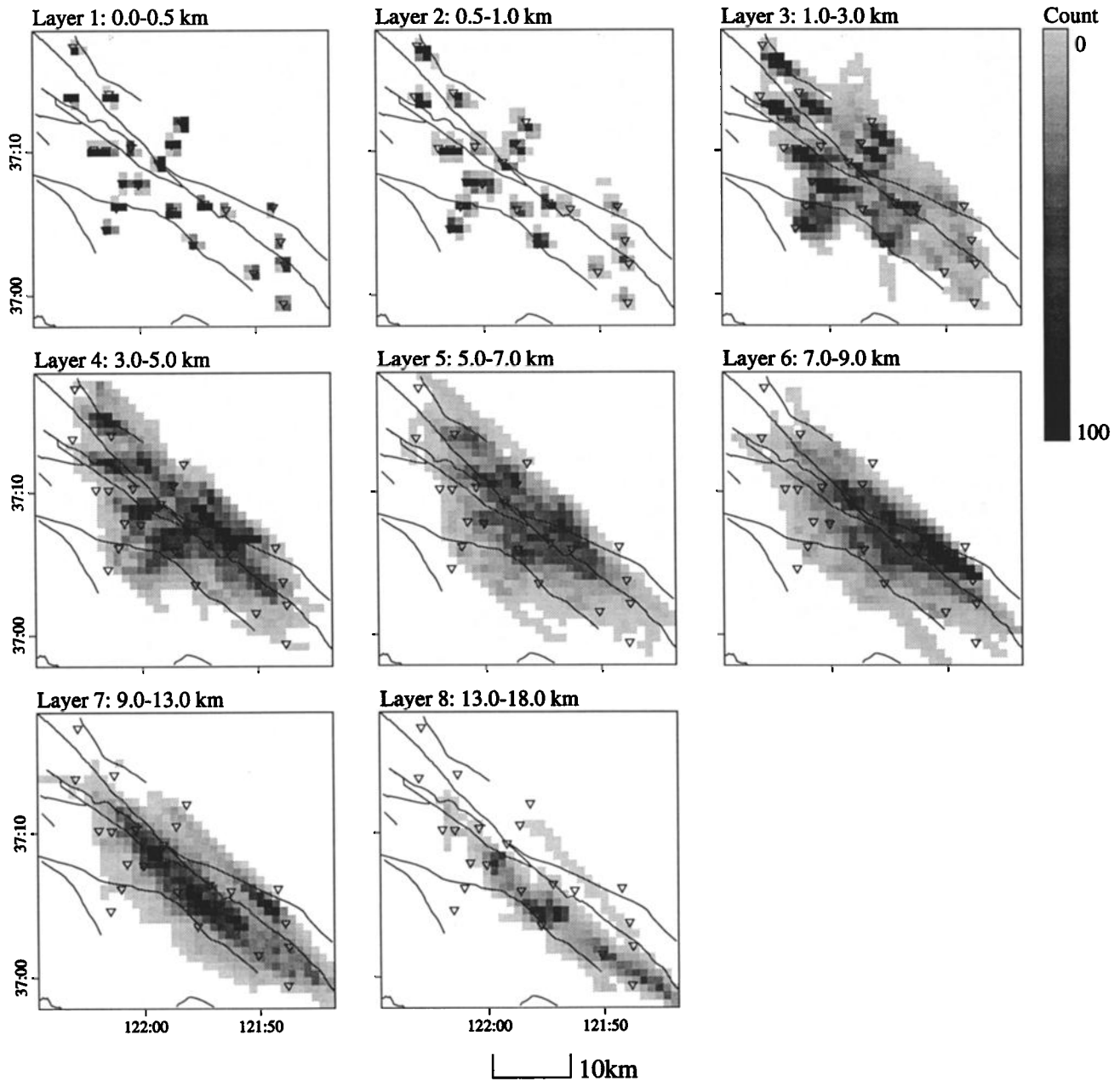
Loma Prieta Coverage

Figure 17. Hit count display showing the density of ray paths per block in the three-dimensional target volume.

course, that both the velocity and attenuation fields are isotropic. If the observed attenuation anomalies are related to anisotropic material properties, associated, for example, with preferred orientations of crack distributions, then we would have to adjust our interpretation accordingly. A much more detailed consideration of the interaction of differentially oriented S waves in the fault zone may help clarify this issue but is beyond the scope of this paper.

It has been suggested that aftershocks occur in more competent (i.e., high Q_p-V_p) parts of the fault zone, places that are able to sustain higher levels of stress prior to rupture. In other sections of the San Andreas fault patterns of high velocity

correlating with dynamic rupture have been observed at Parkfield, [*Lees and Malin*, 1990; *Michael and Eberhart-Phillips*, 1991], North Palm Springs [*Nicholson and Lees*, 1992b] and Landers [*Lees and Nicholson*, 1993; *Nicholson and Lees*, 1992a]. (We note that the narrow (10-20 m wide) low velocity zone observed by some researchers in the Parkfield region of the San Andreas fault [*Li et al.*, 1990], or even a fault zone of a few hundred meters [*Leary and Ben-Zion*, 1992], would be too narrow to have a significant effect on the grosser features of the tomographic analysis presented here.) The anomalous attenuation features perhaps outline a zone of highly competent rocks with elevated Q_p. The lower Q_s may reflect the passage of

waves through a saturated gouge zone where crack alignment decreases Q for S waves.

In volcanic regions, high attenuation has been attributed to hydrothermal activity, highly porous or fractured rocks, or shallow magmatic source areas [*Clawson et al.*, 1989; *Scherbaum and Wyss*, 1990; *Young and Ward*, 1980]. These models agree with physical intuition regarding wave propagation through the anomalous magma accumulations that presumably attenuate seismic signals. Along the San Andreas fault, though, a priori models, based on the assumption that significant fault gouge (>0.5 km thick) causes severe attenuation, fail to predict the observed Q_p structure observed in this study at Loma Prieta. A two-dimensional analysis of a similar data-set by *Guo et al.* [1992] suggested that the P wave attenuation in the fault zone is high, contrary to our analysis. We suspect, however, that Guo et al.'s high-attenuation zone is the region immediately above the lower Q_p zone we have observed and appears as a zone of high Q_p by contrast. Both velocity and attenuation analyses presented here indicate that regions of intense aftershock activity and major dynamic rupture represent stronger material, at least on the scale of structure imaged in this study. The other possibility is that these variations are mainly due to lithologic variations, as proposed by *Shalev* [1993], *Shalev and Lees* [1992], and *Scott* [1992]. *Shalev and Lees* [1992] suggested that the high-velocity anomaly observed in the Loma Prieta region is due to a wedge of buried serpentinite. Serpentinite is a relatively weak material, ubiquitous along the San Andreas fault, which has unusually high V_p/V_s. *Thurber and Atre* [1993], however, did not observe elevated V_p/V_s ratios below 10 km depth between the San Andreas fault and the Zayante faults, although their study has very poor resolution at these depths. While the possibility exists that the high-Q_p/low-Q_s is due to serpentinite, the attenuation properties of this rock type at these confining pressures have not been explored in detail.

Conclusion

Estimates of t* have been used to determine the three-dimensional variations of Q for P and S waves in the Loma Prieta region. We found that constraining the corner frequencies for common source signals changed the overall t* estimates at only a few stations, although variability in the data was reduced. Attenuation of P and S wave signals from high-quality data in the Loma Prieta region show a trend of increasing Q with depth. There is a large-scale body of low Q along a sedimentary basin southwest of the San Andreas fault. High Q_p and low Q_s are observed in the fault zones at depths of 10-18 km, as outlined by aftershock activity. This suggests that pores are fully saturated in the fault zone at depths between 8 and 15 km.

References

Blakeslee, S., Studies in near-surface, crustal and fault zone attenuation: Borehole analysis of Parkfield earthquakes, Ph.D. thesis, Univ. of Calif., Santa Barbara, 1989.

Blakeslee, S., P. Malin, and M. Alvarez, Fault-zone attenuation of high-frequency seismic waves, *Geophys. Res. Lett., 16*(11), 1321-1324, 1989.

Boatwright, J., Detailed spectral analysis of two small New York State earthquakes, *Bull. Seismol. Soc. Am., 68*, 1117-1131, 1978.

Bregman, N. D., C. H. Chapman and R. C. Bailey, Travel time and amplitude analysis in seismic tomography, *J. Geophys. Res., 94*, 7577-7587, 1989.

Brune, J. N., Tectonic stress and the spectra of seismic shear waves from earthquakes, *J. Geophys. Res., 75*, 4997-5009, 1970.

Brune, J. N., Correction: Tectonic stress and the spectra of seismic shear waves from earthquakes, *J. Geophys. Res., 76*, 5002, 1971.

Caceci, M. S., and W. P. Cacheris, Fitting curves to data, *Byte Magazine*, May, 340-360, 1984.

Clawson, S. R., R. B. Smith and H. M. Benz, P wave attenuation of the Yellowstone Caldera from three-dimensional inversion of spectral decay using explosion source seismic data, *J. Geophys. Res., 94*, 7205-7222, 1989.

Eberhart-Phillips, D., V. F. Labson, W. D. Stanley, A. J. Michael and B. D. Rodriguez, Preliminary velocity and resistivity models of the Loma Prieta earthquake region, *Geophys. Res. Lett., 17*(8), 1235-1238, 1990.

Eberhart-Phillips, D., and W. D. Stuart, Material heterogeneity simplifies the picture: Loma Prieta, *Bull. Seismol. Soc. Am., 82*(4), 1964-1968, 1992.

Efron, B., *The Jackknife, the Bootstrap and Other Resampling Plans*, Society for Industrial and Applied Mathematics, Philadelphia, Pa., 1982.

Evans, J. R., and J. J. Zucca, Active high-resolution seismic tomography of compressional wave velocity and attenuation structure at Medicine Lake volcano, northern California Cascade Range, *J. Geophys. Res., 93*, 15,016-15,036, 1988.

Fuis, G. S., and W. D. Mooney, Lithospheric structure and tectonics from seismic-refraction and other data, in The San Andreas fault system, *U. S. Geol. Soc. Prof. Pap. 1515*, 207-236, 1990.

Guo, H., A. Lerner-Lam and D. W. Caress, Anomalous body wave attenuation in the mainshock region of 1989 Loma Prieta, California Earthquake (abstract), *Eos Trans. AGU, 73*(43), Fall Meeting suppl., 368, 1992.

Hanks, T. C., and M. Wyss, The use of body wave spectra in the determination of seismic source parameters, *Bull. Seismol. Soc. Am., 62*, 561-589, 1972.

Ho-Liu, P., H. Kanamori, and R. W. Clayton, Applications of attenuation tomography to Imperial Valley and Coso-Indian Wells region, southern California, *J. Geophys. Res., 93*, 10,501-10,520, 1988.

Leary, P., and Y. Ben-Zion, A 200 M wide fault zone low velocity layer on the San Andreas Fault at Parkfield: Results from analytic waveform fits to trapped wave groups (abstract), *Seismol. Res. Lett., 63*(1), 62, 1992.

Lees, J. M., Tomographic P wave velocity images of the Loma Prieta earthquake asperity, *Geophys. Res. Lett., 17*, 1433-1436, 1990.

Lees, J. M., and R. S. Crosson, Tomographic inversion for three-dimensional velocity structure at Mount St. Helens using earthquake data, *J. Geophys. Res., 94*, 5716-5728, 1989.

Lees, J. M., and P. E. Malin, Tomographic images of P Wave velocity variation at Parkfield, California, *J. Geophys. Res., 95*, 21,793-21,804, 1990.

Lees, J. M., and C. Nicholson, Three-dimensional tomography of the 1992 Southern California sequence: Constraints on dynamic earthquake ruptures?, *Geology, 21*(5), 385-480, 1993.

Lees, J. M., and E. Shalev, On the stability of P wave tomography at Loma Prieta: A comparison of parameterizations, linear and nonlinear inversions, *Bull. Seismol. Soc. Am., 82*(4), 1821-1839, 1992.

Li, Y.-G., P. Leary, K. Aki, and P. Malin, Seismic trapped modes in the Oroville and San Andreas Fault zones, *Science, 249*, 763-766, 1990.

Lindley, G. T., and R. J. Archuleta, Earthquake source parameters and the frequency dependence of attenuation at Coalinga, Mammoth Lakes, and the Santa Cruz Mountains, California, *J. Geophys. Res., 97*, 14,137-14,154, 1992.

Madariaga, R., High frequency radiation from cracks (stress drop) models of earthquake faulting, *Geophys. J., 51*, 625-652, 1977.

Michael, A. J., and D. Eberhart-Phillips, Relations among fault behavior, subsurface geology, and three-dimensional velocity models, *Science*, *253*, 651-654, 1991.

Mooney, W. D., and R. H. Colburn, A seismic-refraction profile across the San Andreas, Sargent, and Calaveras faults, west-central California, *Bull. Seismol. Soc. Am.*, *75*(1), 175-191, 1985.

Nelder, J. A., and R. Mead, A simplex method for function minimization, *Computer J.*, *7*, 308, 1965.

Nicholson, C., and J. M. Lees, 3-D tomographic velocity inversion of the 1992 Landers-Big Bear-Joshua Tree sequence, southern California (abstract), *Eos Trans. AGU*, *73*(43), Fall Meeting suppl., 394, 1992a.

Nicholson, C., and J. M. Lees, Travel-time tomography in the northern Coachella Valley using aftershocks of the 1986 M_L 5.9 North Palm Springs earthquake, *Geophys. Res. Lett.*, *19*(1), 1-4, 1992b.

Paige, C. C., and M. A. Saunders, LSQR: An algorithm for sparse linear equations and sparse least squares, *Trans. Math. Software*, *8*, 43-71, 1982.

Randall, M. J., The spectral theory of seismic sources, *Bull. Seismol. Soc. Am.*, *63*, 1133-1144, 1973.

Scherbaum, F., Combined inversion for the three-dimensional Q structure and source parameters using microearthquake spectra, *J. Geophys. Res.*, *95*, 12,423-12,438, 1990.

Scherbaum, F., and M. Wyss, Distribution of attenuation in the Kaoiki, Hawaii, source volume estimated by inversion of P wave spectra, *J. Geophys. Res.*, *95*, 12,439-12,448, 1990.

Scott, J. S., Microearthquake studies in the Anza Seismic Gap, Ph.D. thesis, Univ. of Calif., San Diego, 1992.

Shalev, E., Three-dimensional seismic investigation of the crust in New Hampshire and Loma Prieta, Ph.D. thesis, Yale Univ., New Haven, Conn., 1993.

Shalev, E., and J. M. Lees, Three-dimensional tomographic analysis at Loma Prieta, *U.S. Geol. Surv. Prof. Pap.*, in press 1994.

Spakman, W., and G. Nolet, Imaging algorithms, accuracy and resolution in delay time tomography, in *Mathematical Geophysics*, edited by N. J. Vlaar et al., 155-187, D. Reidel, Norwell Mass., 1988.

Thurber, C. H., and S. R. Atre, Three-dimensional Vp/Vs variations along the Loma Preita rupture zone, *Bull. Seismol. Soc. Am.*, *83*(3), 717-736, 1993.

Tichelaar, B. W., and L. J. Ruff, How good are our best models: Jackknifing, bootstrapping and earthquake depth, *Eos Trans. AGU*, *70*(20), 593, 1989.

Um, J., and C. Thurber, A fast algorithm for two-point seismic ray tracing, *Bull. Seismol. Soc. Am.*, *77*(3), 972-986, 1987.

Winkler, K., and A. Nur, Pore fluids and seismic attenuation in rocks, *Geophys. Res. Lett.*, *6*, 1-4, 1979.

Wittlinger, G., H. Haessler, and M. Granet, Three-dimensional inversion of Q_p from low magnitude earthquakes analysis, *Ann. Geoph.*, *6*(1), 427-438, 1983.

Young, C. Y., and R. W. Ward, Three-dimensional Q^{-1} model of the Coso Hot Springs known geothermal resource area, *J. Geophys. Res.*, *85*, 2459-2470, 1980.

J. M. Lees, Department of Geology and Geophysics, Yale University, P.O. Box 208109, New Haven CT 06520-8109. (e-mail: lees@lamb.geology.yale.edu)

G. T. Lindley, Institute for Crustal Studies, University of California, Santa Barbara, CA, 93106-1100. (e-mail: grant@crustal.quake.ucsb.edu)